PlexinB1 Inactivation Reprograms Immune Cells in the Tumor Microenvironment, Inhibiting Breast Cancer Growth and Metastatic Dissemination

Giulia Franzolin[1,2], Serena Brundu[1,2], Carina F. Cojocaru[1,2], Aurora Curatolo[1,2], Matteo Ponzo[1], Roberta Mastrantonio[3,4], Emiko Mihara[5], Atsushi Kumanogoh[6,7], Hiroaki Suga[8], Junichi Takagi[5], Luca Tamagnone[3,4], and Enrico Giraudo[1,2]

ABSTRACT

Semaphorin–plexin signaling plays a major role in the tumor microenvironment (TME). In particular, Semaphorin 4D (SEMA4D) has been shown to promote tumor growth and metastasis; however, the role of its high-affinity receptor Plexin-B1 (PLXNB1), which is expressed in the TME, is poorly understood. In this study, we directly targeted PLXNB1 in the TME of triple-negative murine breast carcinoma to elucidate its relevance in cancer progression. We found that primary tumor growth and metastatic dissemination were strongly reduced in PLXNB1-deficient mice, which showed longer survival. PLXNB1 loss in the TME induced a switch in the polarization of tumor-associated macrophages (TAM) toward a pro-inflammatory M1 phenotype and enhanced the infiltration of $CD8^+$ T lymphocytes both in primary tumors and in distant metastases. Moreover, PLXNB1 deficiency promoted a shift in the Th1/Th2 balance of the T-cell population and an antitumor gene signature, with the upregulation of *Icos*, *Perforin-1*, *Stat3*, and *Ccl5* in tumor-infiltrating lymphocytes (TILs). We thus tested the translational relevance of TME reprogramming driven by PLXNB1 inactivation for responsiveness to immunotherapy. Indeed, in the absence of PLXNB1, the efficacy of anti-PD-1 blockade was strongly enhanced, efficiently reducing tumor growth and distant metastasis. Consistent with this, pharmacological PLXNB1 blockade by systemic treatment with a specific inhibitor significantly hampered breast cancer growth and enhanced the antitumor activity of the anti-PD-1 treatment in a preclinical model. Altogether, these data indicate that PLXNB1 signaling controls the antitumor immune response in the TME and highlight this receptor as a promising immune therapeutic target for metastatic breast cancers.

Introduction

Breast cancer (BC) is one of the most frequent tumor types and the most common malignancy in women (1). The tumor microenvironment (TME) is essential to dynamically regulate cancer progression, and due to its influence on the therapeutic outcome, multiple therapies directed to TME components have been developed in the last few years. In particular, several new anticancer approaches target immune cells, e.g., cytotoxic T lymphocytes (to unleash their antitumor properties) or myeloid cells (to block their immune-suppressive activities; ref. 2). A crucial step in the antitumor immune response is the recruitment and activation of adaptive immune cells. In fact, tumors characterized by higher levels of pro-inflammatory cytokines and T-cell infiltrate display a better response to immunotherapy, e.g., immune checkpoint inhibitors (ICI; ref. 3). Hence, turning a "cold" tumor into a "hot" one (in terms of inflammation) has been the focus of many recent efforts in the field. Even though BC is not generally considered a highly infiltrated tumor, the triple-negative BC (TNBC) subtype is characterized by a consistent inflammatory infiltrate and could potentially benefit from immune checkpoint blockade. In line with that, immunotherapy is currently approved as the first line of treatment for a subset of patients diagnosed with advanced TNBC (4).

Semaphorins comprise a large family of evolutionarily conserved proteins. Originally identified as signaling cues for axon navigation, semaphorins are involved in the regulation of diverse biological and pathological processes, from developmental angiogenesis to bone homeostasis and immune responses (5). Plexins comprise a large family of transmembrane receptors for the semaphorins. Accumulating evidence indicates that a number of so-called "immune" semaphorins play a major role in the pathogenesis of immunological diseases and control cancer-associated inflammation, thus representing potential therapeutic targets of interest (6). SEMA4D is a transmembrane semaphorin initially described for its role in the immune system, but it has also been associated with neural development, angiogenesis, and cancer growth (7). Moreover, preclinical

[1]Laboratory of Tumor Microenvironment, Candiolo Cancer Institute, FPO-IRCCS, Candiolo, Italy. [2]Department of Science and Drug Technology, University of Torino, Torino, Italy. [3]Department Life Sciences and Public Health, Università Cattolica del Sacro Cuore, Rome, Italy. [4]Fondazione Policlinico Gemelli–IRCCS, Rome, Italy. [5]Laboratory for Protein Synthesis and Expression, Institute for Protein Research, Osaka University, Osaka, Japan. [6]Department of Immunopathology, Immunology Frontier Research Center, Osaka University, Osaka, Japan. [7]Department of Respiratory Medicine and Clinical Immunology, Osaka University, Osaka, Japan. [8]Department of Chemistry, Graduate School of Science, The University of Tokyo, Tokyo, Japan.

G. Franzolin and S. Brundu contributed equally to this article.

L. Tamagnone and E. Giraudo contributed equally to this work as co-senior authors.

Corresponding Authors: Luca Tamagnone, Department Life Sciences and Public Health, Università Cattolica del Sacro Cuore, Rome 20123, Italy. E-mail: luca.tamagnone@unicatt.it; and Enrico Giraudo, Laboratory of Tumor Microenvironment, Candiolo Cancer Institute, FPO-IRCCS, Candiolo 10060, Italy. E-mail: enrico.giraudo@ircc.it

Cancer Immunol Res 2024;12:1286–301

doi: 10.1158/2326-6066.CIR-23-0289

data suggest that SEMA4D is a key regulator of immune cells in the TME (8, 9). PLXNB1, the main canonical receptor for SEMA4D, is expressed by cancer cells and by multiple players in the TME. For instance, it has been found to control the migration of immature dendritic cells (10) and to sustain B-cell proliferation and survival (11). PLXNB1 expression is also found in endothelial cells (EC), whereby SEMA4D promotes the angiogenic process (12). However, the functional relevance of PLXNB1 in the TME has been so far poorly characterized. Moreover, the intracellular tail of SEMA4D seems to have a signaling role via poorly studied mechanisms (13).

The SEMA4D-targeting monoclonal antibody pepinemab has been tested for clinical use in patients with cancer (14). However, recent findings raised concerns about the safety of targeting SEMA4D in tumors as they revealed increased metastatic spreading in a pancreatic cancer model, possibly due to antibody-mediated retrograde SEMA4D signaling in macrophages (15). In this context, targeting PLXNB1 could represent an alternative way to tackle this signaling axis and to overcome resistance to therapy. Thus, in this study, we evaluated the relevance of PLXNB1 in regulating the TME and tumor progression in mouse models of TNBC. Herein, we unveiled a role for PLXNB1 in the regulation of immune cells in the TME, identifying a potential target to enhance immunotherapy in TNBC.

Materials and Methods

Cell lines

4T1 cells (ATCC Cat# CRL-2539, RRID:CVCL_0125) were purchased from the ATCC in 2015 and cultured in RPMI medium (EuroClone, #ECB9006L) supplemented with 1% L-glutamine (EuroClone, #ECB3000D), 10% FBS (Gibco, #10270-098), and 1% penicillin and streptomycin (EuroClone, #ECB3001D). Py230 cells (ATCC Cat# CRL-3279, RRID:CVCL_AQ08) were purchased from ATCC in 2020 and cultured in F-12K Medium (Kaighn's Modification of Ham's F-12 Medium, ATCC, #30-2004) supplemented with 0.1% MITO+ serum extender (Corning, #355006), 5% FBS (Gibco, #10270-098), and 1% penicillin and streptomycin (EuroClone, #ECB3001D). EMT6 cells (ATCC Cat# CRL-2755, RRID:CVCL_1923) were purchased from ATCC in 2023 and cultured in Waymouth's MB 752/1 Medium (Gibco, #11220-035) supplemented with 15% FBS (Gibco, #10270-098) and 1% penicillin and streptomycin (EuroClone, #ECB3001D). SVEC4-10 cells (RRID:CVCL_4393) were purchased from ATCC in 2005 and cultured in DMEM (EuroClone, #ECB7501L) supplemented with 1% L-glutamine (EuroClone, #ECB3000D), 10% FBS (Gibco, #10270-098), and 1% penicillin and streptomycin (EuroClone, #ECB3001D). HEK-293T cells (RRID: CVCL_0063) were purchased from ATCC in 2019 and cultured in IMDM (Gibco, #21980) supplemented with 1% L-glutamine (EuroClone, #ECB3000D), 10% FBS (Gibco, #10270-098), and 1% penicillin and streptomycin (EuroClone, #ECB3001D). All cell lines were thawed from the initial expansion of the stock, without reauthentication, and used within 10 passages. All cell lines were cultured in a humidified incubator with 5% CO_2 at 37°C. Raji cells and Jurkat cells expressing mFcgRIV were included in the Promega kit (Promega mFcγRIV ADCC Bioassay Kit, #M1201), purchased in 2023; they were used without expansion according to the vendor's request and cultured in RPMI1640 containing 4% low IgG serum (provided with the kit). PlxnB1_4C6 cells derive from a cell clone of Expi293F cells (Thermo Fisher #A14527 RRID:CVCL_D615) stably expressing human PLXNB1 that was established in 2015 as described in ref. 16. The cells, after reviving from the frozen stock, were passaged 20 to 30 times over 3 months, cultured in DMEM (Wako Pure Chemical Co. #041-30081), 10% FCS (Gibco, #10270-098), 1 mg/mL G418 (Nacalai Tesque #16512-52), and 5 μg/mL puromycin (Sigma #P7255), and validated for the high expression levels of human PLXNB1 by flow cytometry. All cell lines were regularly tested for *Mycoplasma* contamination.

Mice and *in vivo* experiments

Six- to eight-week-old female WT BALB/c and C57BL/6 mice were purchased from Charles River. BALB/c *Plxnb1*$^{-/-}$ (C.Cg-*Plxnb1*$^{tm1.1Ltam}$/Cnrm RRID:IMSR_EM:12796), C57BL/6 *Plxnb1*$^{-/-}$ (B6.129-*Plxnb1*$^{tm1.1Ltam}$/Cnrm RRID:IMSR_EM:12800), and BALB/c *Sema4d*$^{-/-}$ (C.cg-*Sema4d*^{tm1Kik}/Cnrm RRID:IMSR_EM:12799) mice were previously generated and described (17, 18). 1×10^6 4T1, 4×10^6 Py230, or 2×10^5 EMT6 cells were orthotopically surgically implanted in the fourth mammary fat pad under anesthesia with 2.5% isoflurane. Tumor growth was monitored by caliper measurement twice a week, and tumor volume was calculated with the formula $(a^2 \times b) \times 0.52$, where a and b stand for the minor and major tumor diameters, respectively. Lung macro-metastasis was counted after counterstaining the airways with Indian ink. For pharmacological treatments, the mice were randomly assigned to different cohorts and treated as described below. Anti-CD8 (Bio X Cell Cat# BE0117, RRID:AB_10950145) was administered intraperitoneally at a dosage of 200 μg at days −1, 0, +1, and +8 (with respect to cancer cell transplantation). Mice were sacrificed at day 15, following the approved animal experimentation protocols, in order to avoid severe adverse effects and the acceleration of tumor progression due to $CD8^+$ cell depletion. Anti PD-1 (Bio X Cell Cat# BE0146, RRID:AB_10949053) was administered intraperitoneally at a dosage of 250 μg every 4 days starting from day 7. For anti-PLXNB1 *in vivo* treatment, an antagonistic PLXNB1-dimerizing protein reported previously [Fc(m6A9)B3; ref. 19] was used. This protein is a human IgG1 Fc-based homodimeric protein grafted with a PLXNB1-binding peptide m6A9 (WRPYIERWTGRLIV) at the tip of E–F loop of the CH3 domain (20). Purified Fc(m6A9)B3 or Fc control was administered intravenously once a week at a dosage of 400 μg/mice, starting 4 weeks post Py230 tumor inoculation or 7 days after EMT6 tumor inoculation. Py230-bearing mice were sacrificed after 3 weeks of treatment with Fc(m6A9)B3, whereas EMT6-bearing mice were sacrificed after 2 weeks. For survival experiments, mice bearing 4T1 and Py230 tumors were euthanized when tumors reached the volume of 700 mm^3 and 500 mm^3, respectively. Biochemical analysis of renal and hepatic function parameters and the hematological profiling of mice was outsourced to the analytical laboratory at the "Clinica Veterinaria Città di Torino". Whole blood was withdrawn from the submandibular vein at sacrifice. All animal procedures were approved by the Ethical Committee of the University of Turin (Candiolo, Turin, Italy) and by the Italian Ministry of Health and were conducted in compliance with European laws and policies.

Immunofluorescence

Tumors from 4T1 or Py230 cells were dissected and collected. Tissues were fresh frozen in OCT (Killik, Bio-Optica, #05-9801) and 10-μm-thick frozen sections were serially cut using a Leica 2135 cryostat. Dried tumor slices were fixed with Zn fixative (0.5 g/L Ca acetate; 5 g/L Zn acetate; 5 g/L Zn chloride; 0.1 mol/L Tris buffer) for 10 minutes and permeabilized with Triton X-100 (Sigma-Aldrich) 0.1% PBS solution. After saturation with 2% goat serum (Vector-D.B.A. #S1000) at room temperature for 1 hour, tumor

slices were incubated overnight with optimized primary antibody dilution, washed, and incubated with appropriate Alexa Fluor-conjugated secondary antibody (Thermo Fisher Scientific Cat# A-21206, RRID:AB_2535792; Cat# A-21434, RRID:AB_2535855; Cat# A-31572, RRID:AB_162543; Cat# A-21208, RRID:AB_2535794; Cat# A-21110, RRID:AB_2535759; Cat# A-21247, RRID:AB_141778; Cat# A-31573, RRID:AB_2536183) for 45 minutes. After staining with DAPI (Roche #10236276001), tumor slices were mounted, and images were acquired with Leica TCS SPE II-DM5500 CSQ confocal microscope equipped with a 20× oil immersion objective lens (ACS APO 20×/0,60 IMM CORR) using Leica LAS AF software. Images (at least four fields/tumor) were acquired with a 20× objective and analyzed using (NIH) ImageJ (RRID:SCR_003070) software. For IF staining, the following primary antibodies were used: anti-CD68 1:100 (Bio-Rad Cat# MCA1957, RRID:AB_322219), anti-CD206 1:100 (R&D Systems Cat# FAB2535G, RRID:AB_10971285), anti-iNOS 1:50 (Abcam Cat# ab15323, RRID:AB_301857), anti-Meca32 1:100 (BD Biosciences Cat# 550563, RRID:AB_393754), anti-Ng2 (Millipore Cat# AB5320, RRID:AB_11213678), anti-CD8 1:100 (Thermo Fisher Scientific Cat# 14-0081-82, RRID:AB_467087), anti-CA9 1:100 (Novus Cat# NB 100-417, RRID:AB_350323), anti-ki-67 1:100 (Thermo Fisher Scientific Cat# MA5-14520, RRID:AB_10979488), anti-CD11c 1:100 (Bio-Rad Cat# MCA1369, RRID:AB_324490), anti-CD8 1:100 (Thermo Fisher Scientific Cat# 14-0081-82, RRID:AB_467087), and anti-GRZB 1:50 (Abcam Cat# ab255598, RRID:AB_2860567).

Flow cytometry

Mouse tumors were cut into small pieces, disaggregated with 1.5 mg/mL type IV collagenase (Worthington, #LS004186) and 100 μg/mL DNase (Sigma-Aldrich, #D5025), and filtered through strainers. 1×10^6 cells were stained with specific antibodies. Tumor-draining lymph nodes were harvested and filtered to obtain a single-cell suspension through a strainer before staining. Cell permeabilization and fixation were performed with the FOXP3/Transcription Factor Staining Buffer Set (eBioscience #00-5523-00). Flow cytometry was performed using the BD LSR Fortessa 20× and analyzed with FlowJo V10 (RRID:SCR_008520) software (absolute cell counts are displayed in Supplementary Table S1). Phenotype analysis was performed with the following antibodies: Fixable Viability Stain 780 (BD Horizon, #565388, RRID:AB_2869673), BV786 Rat Anti-Mouse CD45 (BD Biosciences Cat# 564225, RRID:AB_2716861), BB700 Rat Anti-Mouse Ly-6G (BD Biosciences Cat# 566435, RRID:AB_2739730), BV421 Rat Anti-Mouse Ly-6C (BD Biosciences Cat# 562727, RRID:AB_2737748), BV480 Rat Anti-CD11b (BD Biosciences Cat# 566117, RRID:AB_2739519), PE-CF594 Rat Anti-Mouse F4/80 (BD Biosciences Cat# 565613, RRID:AB_2734770), BB700 Armenian Hamster Anti-Mouse CD3e (BD Biosciences Cat# 566494, RRID:AB_2744393), BB515 Rat Anti-Mouse CD8a (BD Biosciences Cat# 564422, RRID:AB_2738801), BV480 Rat Anti-Mouse CD4 (BD Biosciences Cat# 565634, RRID:AB_2739312), and APC Rat Anti-Mouse IFNγ (BD Biosciences Cat# 554413, RRID:AB_398551). Additionally, the following antibodies were used in some analyses: BUV395 Rat Anti-Mouse CD45 (BD Biosciences Cat# 564279, RRID:AB_2651134), BB700 Armenian Hamster Anti-Mouse CD3e (BD Biosciences Cat# 566494, RRID:AB_2744393), BV605 Rat Anti-Mouse CD8a (BD Biosciences Cat# 563152, RRID:AB_2738030), BUV737 Rat Anti-Mouse CD4 (BD Biosciences Cat# 612844, RRID:AB_2870166), BV480 Rat Anti-Mouse CD25 (BD Biosciences Cat# 566202, RRID:AB_2739593), PE Mouse Anti-Mouse Foxp3 (BD Biosciences Cat# 566881, RRID:AB_2869932), APC Rat Anti-Mouse Granzyme B (Thermo Fisher Scientific Cat# 17-8898-82, RRID:AB_2688068), BV711 Mouse Anti-T-bet (BD Biosciences Cat# 563320, RRID:AB_2738136), BV421 Mouse Anti-GATA3 (BD Biosciences Cat# 563349, RRID:AB_2738152), BUV563 Rat Anti-CD11b (BD Biosciences Cat# 741242, RRID:AB_2870793), PE-CF594 Rat Anti-Mouse F4/80 (BD Biosciences Cat# 565613, RRID:AB_2734770), PE Rat Anti-Mouse CD206 (Thermo Fisher Scientific Cat# MA5-16871, RRID:AB_2538349), FITC Mouse Anti-iNOS/NOS Type II (BD Biosciences Cat# 610331, RRID:AB_397721), and BUV737 Hamster Anti-Mouse CD11c (BD Biosciences Cat# 612797, RRID:AB_2870124).

IHC analysis

IHC for CD8 was performed on formalin-fixed, paraffin-embedded lung sections (10-μm thick) from 4T1 WT and *Plxnb1*$^{-/-}$ mice. Paraffin sections were deparaffinized with xylene and rehydrated with decreasing concentrations of ethanol in water, and the sections were then pretreated with 1% H_2O_2 in methanol for 30 minutes. Antigen retrieval was achieved by heating sections in sodium citrate buffer (pH 6.0) for 6 minutes in a 750-W microwave oven. Tissues were incubated with rabbit anti-CD8 1:100 (Novus Cat# NBP2-29475, RRID:AB_2904552) overnight at 4°C. Samples were then washed and incubated for 1 hour with an anti-rabbit HRP-conjugated secondary antibody (Dako #K4003), and antigens were revealed with 3,3-diaminobenzidine (Dako #K3468) according to the manufacturer's instructions. Sections were counterstained with hematoxylin (Bio-Optica #05-06002L) and visualized with MorphoLens 6 (Morphle) slide scanner at 40×. The expression levels of CD8 were quantified by ImageJ software (RRID:SCR_008520) by analyzing at least four fields/lungs.

Isolation of tumor-infiltrating cell populations

Tumor-infiltrating cell populations were isolated by magnetic separation. Briefly, murine explanted tumors were cut into small pieces, disaggregated with 1.5 mg/mL type IV collagenase (Worthington, #LS004186) and 100 μg/mL DNase (Sigma-Aldrich, #D5025), and filtered through strainers. $CD4^+$ and $CD8^+$ lymphocytes were isolated together after the single-cell suspension was incubated with CD8/CD4 (TIL) Microbeads (Miltenyi, #130-116-480) and magnetically separated using LS Columns (Miltenyi, #130-042-401) accordingly to the manufacturer's instructions. $CD8^+$, $CD4^+$, $CD31^+$, $CD11b^+$, and $F4/80^+$ cells were separated using Miltenyi's #130-116-478, #130-116-475, #130-097-418, #130-126-725, and #130-110-443 microbeads, respectively.

T-cell activation and expansion

T cells were isolated from WT or *Plxnb1*$^{-/-}$ spleens using the Pan T Cell Isolation Kit II (Miltenyi, #130-095-130) accordingly to the manufacturer's instructions. T-cell activation was performed with the mouse T Cell Activation/Expansion Kit (Miltenyi, #130-093-627) in TexMACS Medium (Miltenyi #130-097-196) supplemented with 10% FBS and Mouse IL2 IS 50 U/mL (Miltenyi #130-120-332) for 10 minutes for subsequent Western blot analysis or for 48 hours for subsequent gene expression analysis.

Real-time quantitative PCR analysis of gene expression

RNA was extracted with Maxwell RSC miRNA Tissue Kit (Promega, #AS1460). cDNA preparation was performed according

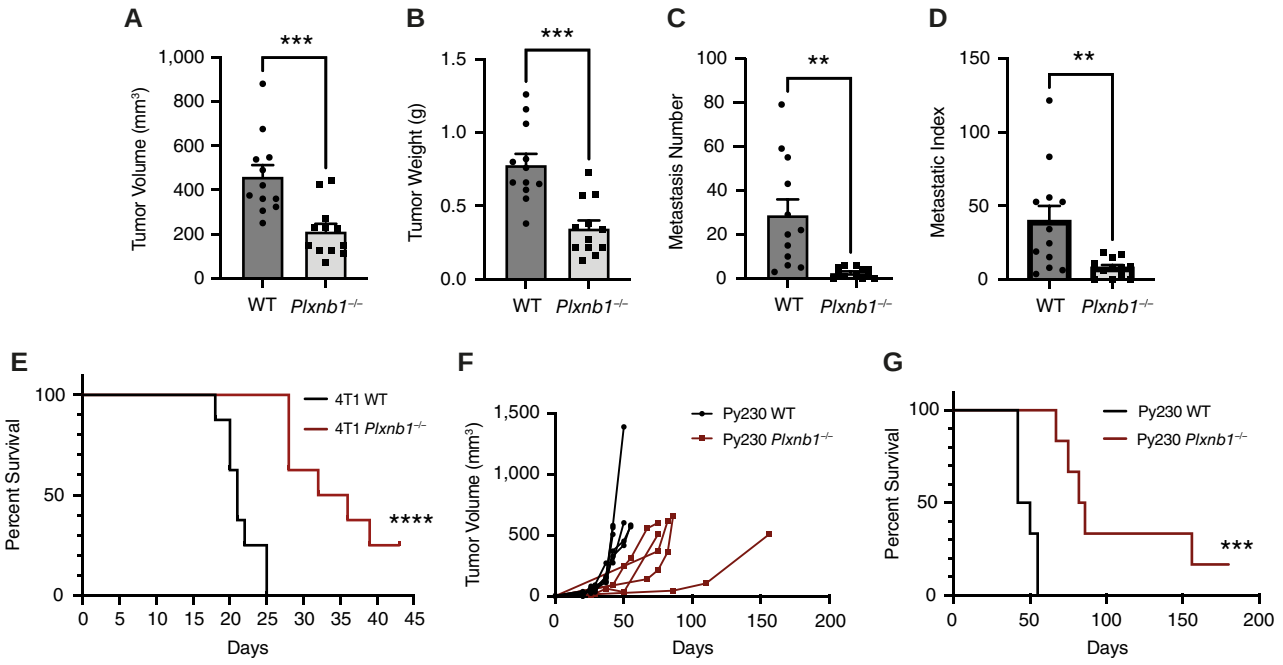

Figure 1.

PLXNB1 expression in the TME sustains tumor growth and metastatic dissemination in TNBC models. **A–E,** *PLXNB1 expression in the 4T1 tumor microenvironment sustains tumor growth, and it is critical for metastatic dissemination.* 1×10^6 4T1 cells were injected in the mammary fat pad of female Balb/c WT and *Plxnb1*$^{-/-}$ mice. Graph bars indicate (**A**) mean tumor volume ± SEM. **B,** mean tumor weight ± SEM. **C,** Mean metastasis number ± SEM. **D,** Mean metastatic index (number of lung metastasis/tumor weight) ± SEM. Results were analyzed by unpaired Student *t* test. **, $P < 0.01$; ***, $P < 0.001$ ($n = 12$ mice). **E,** Survival curve of female 4T1 WT and *Plxnb1*$^{-/-}$ mice injected in the mammary fat pad with 1×10^6 4T1 cells. Animals were euthanized when tumors reached the volume of 700 mm^3. Results were analyzed by log-rank (Mantel–Cox) test, ****, $P < 0.0001$ ($n = 8$ mice). **F** and **G,** *PLXNB1 expression in the Py230 tumor microenvironment supports tumor growth.* **F,** Individual tumor growth curve of C57/BL6 WT and *Plxnb1*$^{-/-}$ mice injected in the mammary fat pad with 4×10^6 Py230 cells ($n = 6$ mice). **G,** Survival curve of female C57/BL6 WT and *Plxnb1*$^{-/-}$ mice injected in the mammary fat pad with 4×10^6 Py230 cells. Animals were euthanized when tumors reached the volume of 500 mm^3. Results were analyzed by log-rank (Mantel–Cox) test, ***, $P < 0.001$ ($n = 6$ mice).

to standard procedures with High-Capacity cDNA Reverse Transcription Kit (Applied Biosystems, #4368814). Gene expression was evaluated by Real-Time PCR using the Taqman Gene Expression Master Mix (Applied Biosystems, #4369016) and the following Taqman probes: PLXNB1 (Mm00555359_m1), SEMA4D (Mm00443147_m1), actin (Mm01205647_g1), PDCD1 (Mm01285676_m1), IL1a (Mm00439620_m1), IL6 (Mm00446190_m1), NOS2 (Mm00440502_m1), TNF (Mm00443258_m1), Arg1 (Mm00475988_m1), CD86: (Mm0044540_m1), IL10 (Mm01288386_m1), MRC1 (Mm01329359_m1), CXCR3 (Mm99999054_s1), GRZB (Mm00442837_m1), IFNg (Mm01168134_m1), Perf1 (Mm01168134_m1), IL2 (Mm00434256_m1), IL12 (Mm0043169_m1), IL4 (Mm00445259_m1), IL5 (Mm00439646_m1), and IL13 (Mm00434204_m1). An average of 30 to 90 ng of template/reaction was used, and the samples were run in triplicate on QuantStudio 7 Pro (Applied Biosystems). Gene expression fold change variations, normalized to β-actin levels and then to a reference control condition, were calculated by the $2^{-\Delta\Delta Ct}$ method. The expression of *Plxnb1* and *Sema4d* mRNAs in different cell types was normalized to the amount of β-actin housekeeping transcripts in each individual sample, by the ΔCt method. The relative counts of specific gene transcripts/10^4 β-actin mRNA molecules (per each sample and cell type) were then calculated by the formula: $2^{-\Delta Ct} \times 10^4$. Gene expression in TILs (isolated as described in "Isolation of tumor-infiltrating cell populations") of targets known to have implications in immune responses was assessed using TaqMan Mouse Immune Array (Applied Biosystems, #4367786). Differential gene expression was considered significant with fold change >2 and $P < 0.05$.

Cell viability assay

4T1, Py230, and EMT6 cells were seeded into 96-well cluster plates (1.500 cell/well) in 5% FBS. Cell viability was evaluated at 24, 48, and 72 hours using the CellTiter-Glo Luminescent Cell Viability Assay (Promega, #G7573) according to the manufacturer's recommendations and using the VICTOR X Multilabel Plate Readers (Perkin Elmer).

In vitro macrophage polarization

Femurs and tibiae of 6-week-old wild-type or *Plxnb1*$^{-/-}$ female BALB/c mice were used to generate bone marrow-derived macrophages (BMDM). Cells were flushed by centrifuging the bones cut at the knee joint. The isolate was filtered through a 40 μm cell strainer, and red blood cells were lysed with RBC Lysis Buffer (BioLegend, #420301). The harvested cells were plated in RPMI medium (EuroClone, #ECB9006L) supplemented with 1% L-glutamine (EuroClone, #ECB3000D), 10% FBS (Gibco, #10270-098), 1% penicillin and streptomycin (EuroClone, #ECB3001D), and 50 ng/mL recombinant mouse CSF (Bio-Techne #416-ML). BMDMs were polarized at day 7 for M1-like polarization using 100 ng/mL LPS (Sigma-Aldrich Cat# L5668) and 200 U/mL mouse

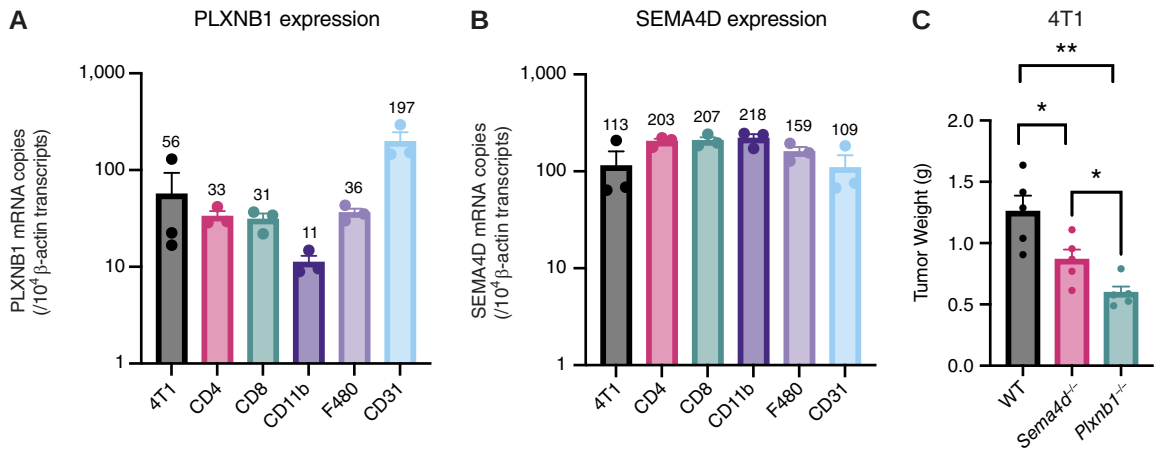

Figure 2.

PLXNB1 and SEMA4D expression in different immune populations of the TME and their contribution on tumor growth in 4T1 mice. **A,** PLXNB1 and (**B**) SEMA4D gene expression evaluated by RT-PCR analysis on RNA extracted from different cell population ($CD4^+$, $CD8^+$, $CD11b^+$, $F4/80^+$, $CD31^+$ cells) purified from 4T1 tumors and in 4T1 cells. Graph bars represent average ± SEM mRNA transcripts per 10^4 β-actin copies, based on triplicate samples per each cell type (see "Materials and Methods" for details). **C,** 1×10^6 4T1 cells were injected in the mammary fat pad of female Balb/c WT, *Sema4d*$^{-/-}$, and *Plxnb1*$^{-/-}$ mice. Graph bars indicate mean tumor weight ± SEM. Results were analyzed by unpaired Student *t* test. *, $P < 0.05$; **, $P < 0.01$ ($n = 5$ mice).

IFNγ (Miltenyi, #130-105-785). To obtain the M2-like phenotype, we used 20 ng/mL mouse IL-4 (Sigma-Aldrich Cat# I1020). BMDMs were polarized for 24 hours.

Gene transfer

Nonreplicating viral particles containing the targeted shRNA for *Plxnb1* TRCN0000078913 from Sigma Mission Library (or empty vector pLKO.1 noncoding plasmids) were produced in HEK-293T (RRID: CVCL_0063) packaging cells by co-transfection of the transfer vector, of the packaging plasmids pCMVΔR8.74, of the pRSV.REV plasmid, and of the vesicular stomatitis virus (VSV) envelope plasmid pMD2.VSV-G using the calcium phosphate precipitation method as previously described (21). Target cells were then incubated with the conditioned media derived from transfected HEK-293T (RRID: CVCL_0063) cells, in the presence of 8 μg/mL polybrene (Merk, #H9268-5G), for 8 to 12 hours. Red fluorescent protein (RFP)-expressing 4T1 cells were generated by infection with lentiviral particles encoding Turbo-RFP (BPS Bioscience # 78347-P).

Tumor cell extravasation assay

For *in vivo* extravasation assays, 1×10^6 RFP-expressing 4T1 cells were injected into the lateral mouse tail vein of 6- to 8-week-old WT and *Plxnb1*$^{-/-}$ BALB/c mice. Mice were sacrificed 48 hours after injection, and their lungs were perfused with PAF 4% (ChemCruz; #sc-281692). RFP detection was performed with LEICA DMI3000 B fluorescence microscope equipped with a 20× objective lens (Leica, HI PLAN 20×/0,40 PH1) and acquired with Photometrics Cool SNAP HQ camera. Quantification of metastatic cells in the lungs was done by analyzing at least four microscopic fields per lung, using (NIH) ImageJ (RRID: SCR_003070) software.

Adhesion assay

SVEC4-10 (RRID:CVCL_4393) ECs were plated at a density of 2.5×10^5 in 9.6 cm^2 wells, the day before the experiment. 4T1 cancer cells were labeled with Vybrant DID cell-labeling solution (Life Technologies, #V22887) according to the manufacturer's instructions. Labeled cells were gently detached with 1 mmol/L EDTA and plated on sub-confluent EC layers. Cancer cells were let to adhere for 30 minutes at 37°C and 5% CO_2 and then washed 3 times with PBS. Images were acquired immediately with a DMI4000 B Leica optical microscope equipped with a 10× objective lens. (Leica, HCX FL PLAN 10X/0.25) at 10× magnification and analyzed using (NIH) ImageJ (RRID:SCR_003070) software.

Western blot

Cells were lysed in RIPA buffer supplemented with 1 mmol/L Na_3VO_4 and protease inhibitor cocktail (Sigma-Aldrich, #P8340). Protein concentration of cell extracts was determined using Pierce bicinchoninic acid (BCA) reagent (Thermo Fisher Scientific, #23227) according to the manufacturer's instructions. Protein samples were denaturated by adding a 4× loading buffer (β-mercaptoethanol 0.6 mol/L; SDS 8%; Tris-HCl 0.25 mol/L pH 6,8; glycerol 40%; bromophenol blue 0.2%) and incubated at 95°C for 5 minutes. Samples containing equivalent amounts of protein were subjected to 7.5% SDS-PAGE. Proteins were transferred onto a nitrocellulose membrane using the Trans-Blot Turbo Transfer System (Bio-Rad) according to manufacturer's instructions, probed with antibodies targeting proteins of interest, and antibody binding was revealed by enhanced chemiluminescence technique using a ChemiDoc Image Lab analyzer and software (Bio-Rad), according to the manufacturer's protocols. Approximately 10% BSA was used for filter blocking in all conditions. The following antibodies were used: totAKT (Cell Signaling Technology Cat# 9272, RRID:AB_329827), pAKT (Cell Signaling Technology Cat# 9271, RRID:AB_329825), totSTAT3 (Santa Cruz Biotechnology Cat# sc-8019, RRID:AB_628293), p-Stat3 (Santa Cruz Biotechnology Cat# sc-8059, RRID: AB_628292), and vinculin (Sigma-Aldrich Cat# V9131, RRID: AB_477629).

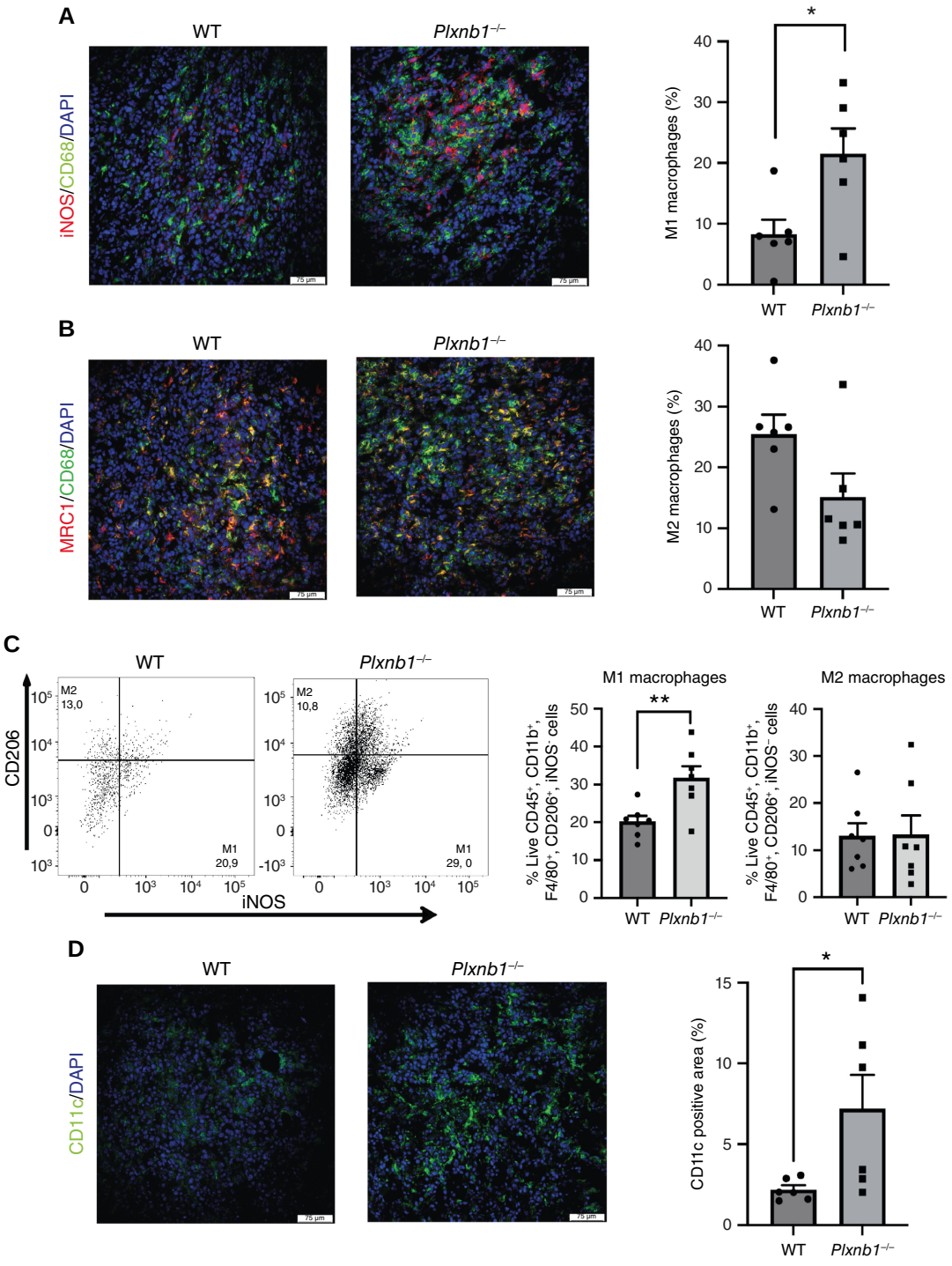

Figure 3.

PLXNB1 depletion enhances M1-like macrophages in the TME and CD11c$^+$ APC infiltration. **A–C,** *PLXNB1* deficiency reprograms macrophages toward a M1 pro-inflammatory phenotype. Representative images of (**A**) CD68 (green) and iNOS (red) or (**B**) CD68 (green) and MRC1 (red) immunofluorescence staining of 4T1 tumors from WT and *Plxnb1*$^{-/-}$ tumors. In **A** and **B** M2 and M1 polarization was evaluated, respectively, as the percentage of MRC1 or iNOS fluorescence signal overlapping the CD68 channel using ImageJ "colocalization" plugin and normalized to total macrophage area ± SEM. Results were analyzed by unpaired Student *t* test. *, $P < 0.05$ ($n = 6$ tumors). Scale bars, 75 μm. **C,** Representative dot plots of whole 4T1 tumor digests analyzed with flow cytometry. Graph bars represent the percentage of CD206$^+$ or iNOS$^+$ on F4/80$^+$ cells, gated on CD11b$^+$ and CD45$^+$ live cells. Results were analyzed by unpaired Student *t* test. **, $P < 0.01$ ($n = 7$ tumors). **D,** *Increased number of infiltrating CD11c$^+$ APCs in tumors grown in Plxnb1*$^{-/-}$ *mice.* CD11c immunofluorescence staining of 4T1 tumors from WT and Plxnb1$^{-/-}$ tumors. CD11c immunofluorescence staining quantification, measured as a positive area percentage (%) ± SEM. Results were analyzed by unpaired Student *t* test. *, $P < 0.05$ ($n = 6$ tumors). Scale bars, 75 μm.

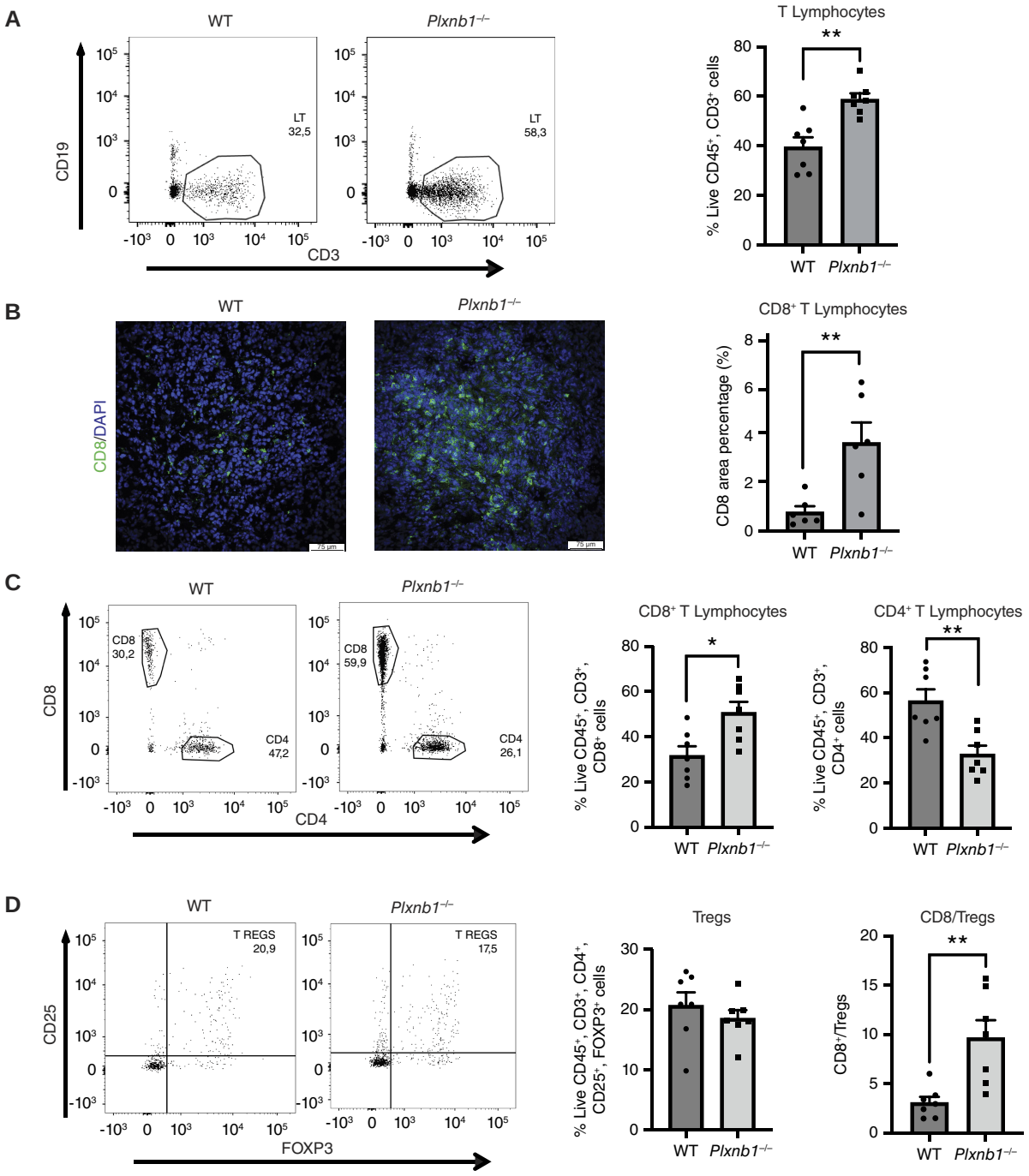

Figure 4.

PLXNB1 depletion induces cytotoxic CD8$^+$ T-cell recruitment in the TME and a shift toward a Th1 phenotype. **A,** Representative dot plots of 4T1 whole tumor digests analyzed with flow cytometry. Graph bars represent the percentage of CD3$^+$ cells on CD45$^+$ live cells ($n = 7$ tumors). **B,** CD8 immunofluorescence staining of 4T1 tumors from WT and *Plxnb1*$^{-/-}$ mice ($n = 6$ tumors). Scale bars, 75 μm. **C,** Representative dot plots of 4T1 whole tumor digests analyzed with flow cytometry. Graph bars represent the percentage of CD8$^+$ or CD4$^+$ on CD3$^+$ cells, gated on CD3$^+$ and CD45$^+$ live cells ($n = 7$ tumors). **D,** Representative dot plots of 4T1 whole tumor digests analyzed with flow cytometry. Graph bars represent the percentage of CD25$^+$ and Foxp3$^+$ on CD4$^+$ T cells, gated on CD3$^+$ and CD45$^+$ live cells ($n = 7$ tumors). (*Continued on the following page.*)

Antibody-dependent cellular cytotoxicity (ADCC) assay

ADCC activity was evaluated using the Promega mFcγRIV ADCC Bioassay Kit (Cat#M1201) according to the manufacturer's instruction. The anti-CD20 (mouse IgG2a class antihuman CD20 antibody) was provided with the kit. Fc(m6A9)B3-elicited ADCC was tested using human PlexinB1-expressing stable cells [clone 4C6,

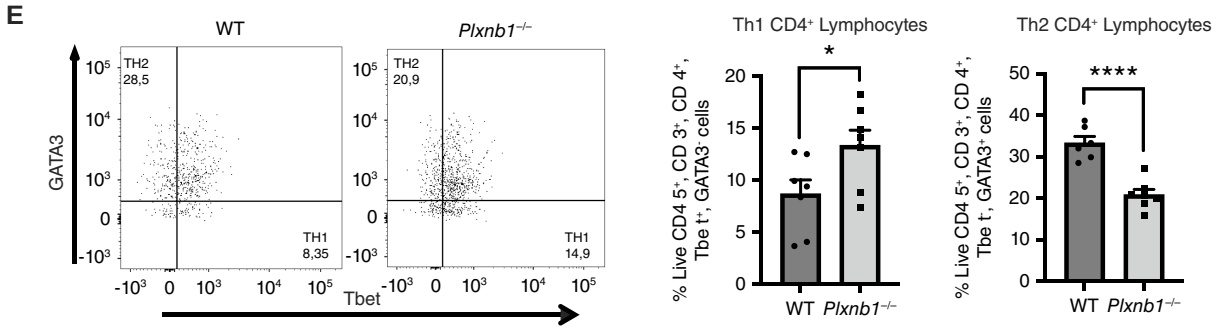

Figure 4.

(*Continued.*) **E,** Representative dot plots of 4T1 whole tumor digests analyzed with flow cytometry. Graph bars represent the percentage of Tbet$^+$ (Th1) and Gata3$^+$ (Th2) on CD4$^+$ T cells, gated on CD3$^+$ and CD45$^+$ live cells ($n = 7$ tumors). Results were analyzed by unpaired Student *t* test. *, $P < 0.05$; **, $P < 0.01$; ****, $P < 0.0001$.

established previously (16)] as the target cells. Briefly, 1×10^4 target cells (Raji or PlxB1_4C6) were plated in a 96-well plate together with increasing concentrations of test compounds and 7.5×10^4 cells/well effector cells (Jurkat cells expressing mouse FcγRIV), followed by incubation for 6 hours at 37°C and 5% CO_2. After the addition of the substrate (Bio-Glo Reagent), luminescence was measured using a GloMax Navigator.

Statistical analyses

The statistical significance of quantitative data was analyzed by GraphPad Prism (RRID:SCR_002798) 10.0.0 software, applying the most appropriate methods and correction tests, specified in individual figure legends. Statistical tests used in this study were as follows: unpaired *t* test, log-rank (Mantel–Cox) test, and two-way ANOVA test. $P < 0.05$ was considered significant. *, $P < 0.05$; **, $P < 0.01$; ***, $P < 0.001$; ****; $P < 0.0001$.

Data availability

The data generated in this study are available in the manuscript and its supplementary files or upon request from the corresponding author.

Results

PLXNB1 expression in the TME sustains tumor growth and metastatic dissemination in TNBC models

In order to assess the role of PLXNB1 in the TME, we performed *in vivo* orthotopic tumor transplants of the murine TNBC model 4T1 in syngeneic WT and PLXNB1-deficient animals (*Plxnb1*$^{-/-}$ mice). The ability of 4T1 cells to develop tumors was significantly reduced when they were transplanted in the mammary fat pad of *Plxnb1*$^{-/-}$ mice compared with WT controls (**Fig. 1A** and **B**). Next, we evaluated the role of PLXNB1 expression in the TME for the metastatic process and found that 4T1 tumors growing in *Plxnb1*$^{-/-}$ mice gave rise to fewer macrometastasis in the lungs compared with those growing in a WT environment (**Fig. 1C**). Tumors grown in PLXNB1-deficient animals also displayed a significantly lower metastatic index, defined as the number of lung metastasis normalized to the primary tumor weight (**Fig. 1D**). This was confirmed also when analyzing tumors of comparable size, indicating that the reduced metastatic burden was not simply a result of a lesser primary tumor mass (Supplementary Fig. S1A). In addition, to assess whether PLXNB1 inhibition would also enhance mice survival, we set up an experiment in which we predefined an end point for sacrifice. In this context, we observed enhanced survival in tumor-bearing *Plxnb1*$^{-/-}$ mice compared with WT controls (**Fig. 1E**). The same effect on tumor progression of PLXNB1 deficiency was observed in another *in vivo* orthotopic TNBC model, by transplanting Py230 cancer cells in syngeneic C57/BL6 mice. In fact, although showing different and slower growth kinetics compared with 4T1 (22), Py230 BC cells injected in the mammary fat pad of female *Plxnb1*$^{-/-}$ mice displayed a significant delay in tumor growth, compared with those grown in WT mice (**Fig. 1F**), and this was then associated with increased survival (**Fig. 1G**).

A short-term metastatic dissemination assay revealed no significant differences between WT and PLXNB1-deficient mice (Supplementary Fig. S1B). SEMA4D is known to participate in monocyte–EC adhesion via coupling with PLXNB receptors (23). Although we observed that SEMA4D was expressed by 4T1 cancer cells (Supplementary Fig. S1E) and PLXNB1 is known to be highly expressed by EC (12), no differences in 4T1 cancer cell adhesion were observed in *Plxnb1*-silenced EC (Supplementary Fig. S1C). These data indicate that the reduced ability of 4T1 cells to metastasize from primary tumors is not accounted for by differences in their ability to extravasate in the lungs or to adhere to the EC, thus suggesting that other mechanisms account for the effect of *Plxnb1* silencing on TNBC progression and metastatic dissemination.

PLXNB1 is expressed in different immune cell populations in the TME of 4T1 tumors

To understand the mechanisms of PLXNB1-dependent regulation of tumor progression, we first assessed the distribution of PLXNB1 and its main ligand SEMA4D in the TME of 4T1 tumors. Thus, we purified endothelial, myeloid, and lymphoid cells from tumor samples, and, by means of real-time PCR, we analyzed the expression levels of these transcripts. In line with previous literature (12), we found that PLXNB1, besides its expression in cancer cells, is highly expressed in EC of 4T1 tumors (**Fig. 2A**; Supplementary Fig. S1D). Furthermore, PLXNB1 was detectably expressed both in CD4$^+$ and CD8$^+$ T cells and myeloid cells in the TME (**Fig. 2A**). Similarly, SEMA4D was expressed both in T lymphocytes and myeloid cells, as previously shown (7–9) at a comparable level as in EC (**Fig. 2B**). Because SEMA4D

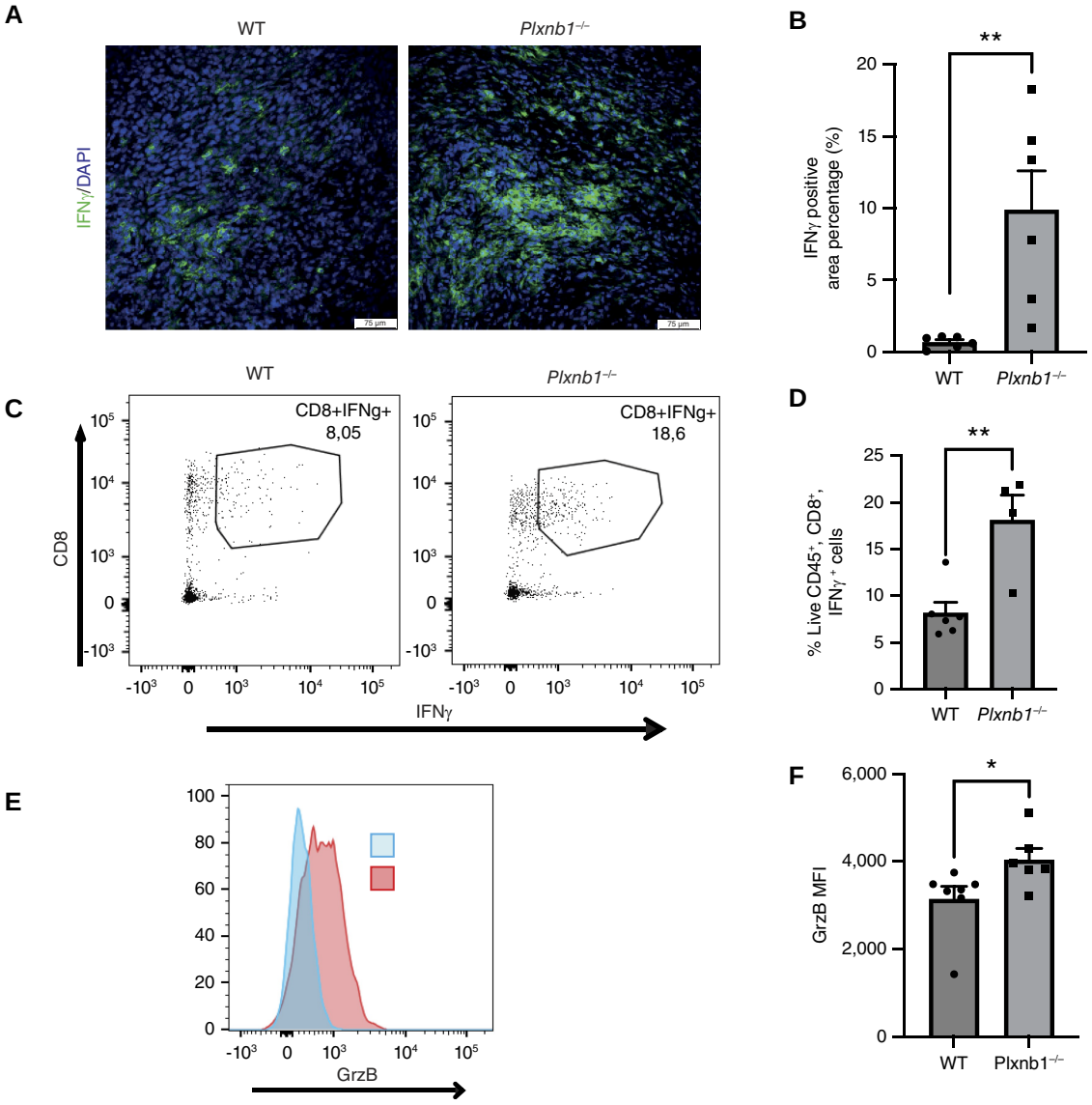

Figure 5.

PlexinB1 deficiency activates and reprograms T cells toward an antitumor phenotype. **A–D,** *Increased levels of IFNγ in the TME of Plxnb1*$^{-/-}$ *mice.* **A,** IFNγ immunofluorescence staining of 4T1 tumors from WT and *Plxnb1*$^{-/-}$ mice. **B,** IFNγ immunofluorescence staining quantification was measured as a positive area percentage (%) ± SEM. Results were analyzed by unpaired Student *t* test. **, $P < 0.01$ ($n = 6$ tumors). Scale bars, 75 μm. **C,** Representative dot plots of 4T1 whole tumor digests analyzed with flow cytometry for $CD8^+$ T cells and IFNγ. **D,** Graph bars represent the percentage of $IFN\gamma^+$ $CD8^+$ T cells on $CD3^+$ cells, gated on $CD45^+$ live cells ($n =$ at least 4 tumors). Results were analyzed by unpaired Student *t* test. **, $P < 0.01$. **E** and **F,** *Increased levels of GrzB in the TME of Plxnb1*$^{-/-}$ *mice.* **E,** Representative histograms of $CD8^+$ T-cell GrzB expression. **F,** MFI was assessed in flow cytometry. Results were (*Continued on the following page.*)

inhibition has been shown to have an impact on tumor growth in diverse mouse models (7, 8), and it is currently assessed for therapeutic purposes in patients with cancer (8, 9, 24), we wished to compare the impact of SEMA4D or PLXNB1 loss on tumor progression in our mouse models. To this end, we analyzed the growth of 4T1 tumor cells orthotopically implanted in *Sema4d*$^{-/-}$, *Plxnb1*$^{-/-}$, and WT mice. Although we detected a significant reduction of the tumor burden in both knockout mouse strains, compared with WT mice, tumor growth suppression was significantly greater in *Plxnb1*$^{-/-}$ mice (**Fig. 2C**).

PLXNB1 depletion promotes tumor vessel normalization and reduces tumor hypoxia

The PLXNB1-ligand SEMA4D is a well-recognized pro-angiogenic factor (12), and tumor-induced angiogenesis is impaired in SEMA4D-deficient mice (7). We hence hypothesized that the reduced primary tumor growth and metastatic dissemination observed in *Plxnb1*$^{-/-}$ mice could be explained in part by impaired tumor angiogenesis. Confocal microscope analysis of EC of tumor sections did not indicate a significant reduction in tumor vessel area of *Plxnb1*$^{-/-}$ compared with WT mice, indicating that tumor-

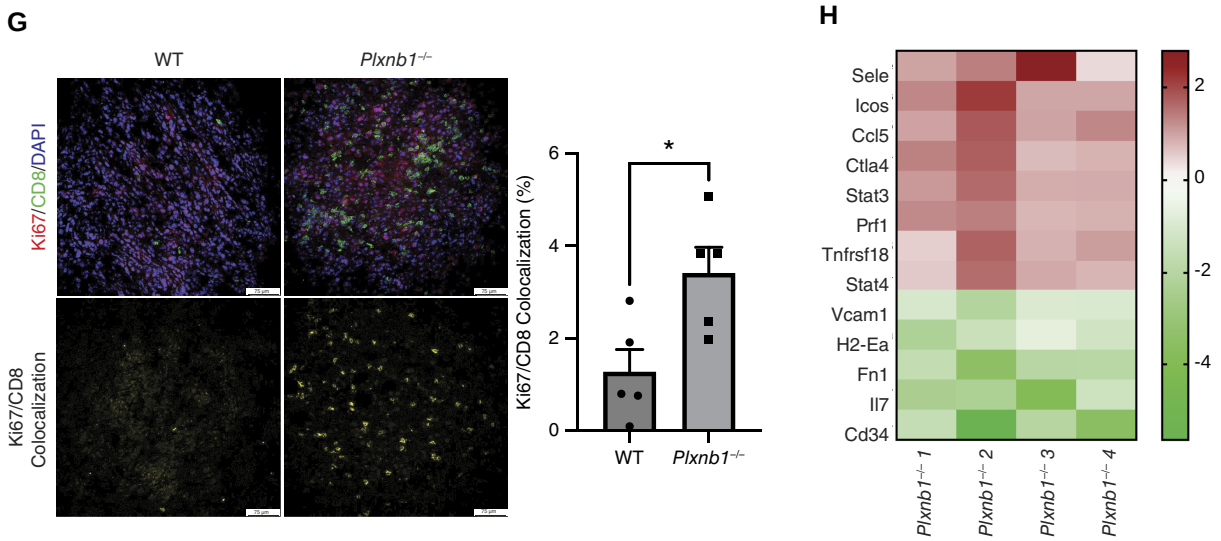

Figure 5.

(*Continued.*) analyzed by unpaired Student *t* test. *, $P < 0.05$ ($n =$ at least 6 tumors). **G,** *$CD8^+$ T-cell proliferation is increased in Plxnb1$^{-/-}$ mice.* Representative images of IF staining of 4T1 tumors from WT and *Plxnb1*$^{-/-}$ tumors for CD8 in green and Ki67 in red. Ki67/CD8 colocalization signal, shown in yellow, was evaluated using ImageJ "colocalization" plugin and normalized to total CD8 area. Results were analyzed by unpaired Student *t* test. *, $P < 0.05$. Scale bars, 75 μm ($n = 5$ tumors). **H,** *Transcriptional changes induced by PlexinB1 deficiency in TILs.* Heatmap representation of the most up- and downregulated genes identified by the Taqman Mouse Immune Array (fold change >2 and $P < 0.05$). Color gradient represents a $\log_2$ fold change scale.

induced angiogenesis was not reduced (Supplementary Fig. S2A and S2B). We did observe a higher degree of pericyte coverage of tumor vessels in *Plxnb1*$^{-/-}$ mice, compared with the WT, as assessed by co-immunostaining of tumor sections for EC and pericyte markers (Meca32 and NG2, respectively; Supplementary Fig. S2A and S2C). Increased pericyte recruitment to tumor vessels indicates that *Plxnb1*$^{-/-}$ mice tumor vasculature is more mature, displaying a phenotype previously described as "normalized" (25). We then wondered if the increase in vessel coverage observed in *Plxnb1*$^{-/-}$ mice was functionally relevant in terms of vascular normalization. In tumors grown in PLXNB1-deficient mice, we observed a significant reduction of tumor hypoxia markers, e.g., lower levels of carbonic anhydrase IX (CAIX; Supplementary Fig. S2D), a well-known hypoxia-inducible enzyme that has been previously associated with acidosis, invasiveness, and drug resistance (26). These data show an unexpected impact of PLXNB1 inactivation, different from that of its best-known ligand SEMA4D, to induce tumor vessel normalization and efficiently reduce tumor hypoxia, which is widely considered a tumor-inhibiting mechanism (25).

PLXNB1 deficiency enhances the amount of M1-like macrophages and dendritic cells in the TME

Antibody-mediated targeting of SEMA4D enhances the recruitment of activated monocytes and lymphocytes to the tumor site, thus skewing the balance of stromal cells and cytokines in the TME toward an antitumor environment (8, 9). Hence, we investigated immune cell recruitment in the TME of *Plxnb1*$^{-/-}$ and WT mice. We observed an overall increase of infiltrating $CD68^+$ macrophages in tumors grown in PLXNB1-deficient mice compared with those grown in WT mice (Supplementary Fig. S3A). We furthermore investigated the polarization state of infiltrating macrophages and found that PLXNB1 deficiency caused a shift from an M2-like (protumoral) to an M1-like (antitumoral) prevalent phenotype, compared with controls (**Fig. 3A–C**). To further investigate the major myeloid cell subtype recruited to tumors, we assessed infiltrating dendritic cells ($CD11c^+$ cells). We observed increased numbers of $CD11c^+$ cells in the tumor stroma of PLXNB1-deficient mice compared with controls (**Fig. 3D**). To further assess the effect of PLXNB1 depletion on macrophage polarization, we set up a series of experiments by purifying myeloid cells from the bone marrow of *Plxnb1*$^{-/-}$ and WT mice, followed by treatments inducing macrophage polarization. PLXNB1-deficient BMDMs showed downregulated expression of Arg-1 (M2 marker) and a trend toward an upregulation of iNOS (M1 marker) compared with WT counterparts (Supplementary Fig. S3C and S3D). These data are in line with our observations in tumor tissues demonstrating a switch from an M2-like toward an M1-like macrophage phenotype in 4T1 *Plxnb1*$^{-/-}$ versus WT tumors.

PLXNB1 deficiency induces cytotoxic $CD8^+$ T-cell recruitment in the TME and a shift toward Th1 phenotype

Based on the observed shift in macrophage polarization, we next analyzed the adaptive immune response, by assessing the presence, activation, and co-stimulation of lymphoid cells, which are required to develop a successful antitumor immune response (27). In particular, we investigated the differential recruitment of TILs in the TME of WT and *Plxnb1*$^{-/-}$ mice. Although we did not observe significant changes in T-cell or dendritic cell populations in draining lymph nodes (Supplementary Fig. S4), we detected an increased number of $CD3^+$ T lymphocytes in the primary tumors grown in *Plxnb1*$^{-/-}$ mice (**Fig. 4A**). We also observed enhanced cytotoxic $CD8^+$ T-cell recruitment in *Plxnb1*$^{-/-}$ TME compared with WT controls (**Fig. 4B** and **C**), further highlighted by an increase of infiltrating $CD8^+$ along with a reduction of $CD4^+$ lymphocytes in *Plxnb1*$^{-/-}$ mice (**Fig. 4C**). Consistent with what was seen in the

primary tumors, we found enhanced recruitment of $CD8^+$ T cells in lung metastases of tumors grown in *Plxnb1*$^{-/-}$ mice compared with WT controls (Supplementary Fig. S5D and S5E).

We also analyzed the $CD4^+$ T-cell populations in the primary tumors, observing that the immunosuppressor regulatory T cell (Treg) subset of $CD4^+$ T cells was unchanged in *Plxnb1*$^{-/-}$ mice compared with WT controls (**Fig. 4D**), thereby implying an increased ratio of $CD8^+$/Treg cells (**Fig. 4D**). Further assessment of the phenotype of $CD4^+$ T cells showed a significant reprogramming toward a Th1 polarization state (**Fig. 4E**).

PLXNB1 deficiency activates and reprograms T cells toward an antitumor phenotype

It has been shown previously that 4T1 cells show greater capacity to grow tumors and metastasize when transplanted into IFNγ$^{-/-}$ mice (28). We found increased levels of IFNγ in tumors grown in *Plxnb1*$^{-/-}$ mice (**Fig. 5A** and **B**). Because cytotoxic $CD8^+$ T cells, which we found to be increased in the TME of *Plxnb1*$^{-/-}$ mice, are a major source of IFNγ, we aimed at identifying IFNγ-producing cells in our tumors. Indeed, infiltrating *Plxnb1*$^{-/-}$ $CD8^+$ T cells produced higher levels of IFNγ compared with their WT counterparts (**Fig. 5C** and **D**). Indicative of their functional activation, we found increased intratumoral proliferation of $CD8^+$ cytotoxic T cells in 4T1 tumors grown in *Plxnb1*$^{-/-}$ mice compared with WT controls (**Fig. 5G**); moreover, PLXNB1 deficiency was associated with an enhanced production of the protein GrzB (**Fig. 5E** and **F**). Furthermore, phenotypic analysis revealed that *Plxnb1*$^{-/-}$ and WT cytotoxic T cells maintained the expression of the immune checkpoint inhibitor PD-1 (Supplementary Fig. S5A). Thus, to get further insights into cancer immunity associated with PLXNB1 deficiency, we measured the expression of immune response genes in TILs purified from 4T1 tumors growing in *Plxnb1*$^{-/-}$ and WT mice (**Fig. 5H**). An array analysis identified 13 (out of 96) genes that were significantly differentially expressed. Among the most upregulated genes in *Plxnb1*$^{-/-}$ TILs were well-known positive regulators and effectors of T-cell responses, such as the inducible T-cell co-stimulatory receptor (*Icos*; ref. 29), the effector protein Perforin1 (*Prf1*; ref. 30), transcription factors *Stat3* and *Stat4*, chemokines such as *Ccl5* (31), and E-selectin (*Sele*). Among the top down-modulated genes, we found *Vcam1*, the extracellular matrix component *Fn1*, and *Cd34*. Consistent with this, we found increased STAT3 and AKT signaling in *ex vivo* activated T cells derived from *Plxnb1*$^{-/-}$ mice compared with T cells derived from WT mice (Supplementary Fig. S5B). To further assess the effect of PLXNB1 deficiency on T-cell phenotype, we performed gene expression analysis of $CD4^+$/$CD8^+$ T cells purified from the spleens of *Plxnb1*$^{-/-}$ or WT mice, and these activated and expanded *in vitro*. We observed an upregulation of IFNγ and IL10 mRNA levels in *Plxnb1*$^{-/-}$ T cells compared with WT counterparts (Supplementary Fig. S5C), suggesting that PLXNB1 targeting renders T cells more inclined to immune activation. Together, these data suggest that PLXNB1 deficiency in the 4T1 TME leads to a significant recruitment of $CD8^+$ T cells programmed toward an antitumor phenotype.

PLXNB1 inactivation enhances the efficacy of anti-PD-1 immunotherapy in tumor-bearing mice

Given the strong impact of environmental PLXNB1 deficiency in increasing recruitment and activation of $CD8^+$ cytotoxic T cells, we assessed the functional importance of their antitumor activity in *Plxnb1*$^{-/-}$ mice by inactivating these cells with depleting CD8-specific antibodies. In this experiment, the mice were sacrificed after 2 weeks of treatment to avoid adverse effects due to acceleration of tumor progression upon $CD8^+$ cell depletion. The depletion of $CD8^+$ T cells nullified the tumor- and metastasis-suppressive effect due to PLNXB1 deficiency, strongly suggesting that the activity of these cells is enhanced in *Plxnb1*$^{-/-}$ mice (**Fig. 6A–C**). It is known that increased levels of infiltrating TILs correlate with good prognosis in patients with TNBC, even in the absence of adjuvant therapy (32). Given the strong increase in the number and activation of infiltrating TILs observed in the *Plxnb1*$^{-/-}$ TME and their critical functional role, we sought to investigate whether the combination of PLXNB1 deficiency in the TME with treatment with an ICI, such as an anti-PD-1, could achieve a greater effect in inhibiting tumor progression in mice. Indeed, whereas PD-1 blockade in 4T1 tumors engrafted in WT mice barely reduced primary tumor size, in *Plxnb1*$^{-/-}$ mice, anti-PD-1 treatment almost achieved complete tumor rejection (**Fig. 6D–F**). As shown above, the number of lung metastases was lower in *Plxnb1*$^{-/-}$ mice compared with controls, but anti-PD-1 treatment further reduced the number of metastasis in *Plxnb1*$^{-/-}$ mice only. These results show that $CD8^+$ T-cell activation induced by PLXNB1 inactivation in the TME enhances the efficacy of immunotherapy, providing the rationale for combining PLXNB1-blocking drugs with ICIs, in TNBC.

Pharmacological inhibition of PLXNB1 efficiently hampers tumor growth and enhances the antitumor effect of anti-PD-1 therapy

To better assess the potential clinical application of PLXNB1 inhibition in the treatment of TNBC, we assessed the antitumor efficacy of systemic delivery of a recently developed protein inhibitor of PLXNB1 signaling, Fc(m6A9)B3. This is an Fc-based engineered protein with a PLXNB1-binding peptide moiety, which can strongly antagonize ligand-induced PLXNB1 activation by dimerizing cell surface PLXNB1 in a signaling incompetent conformation (19). The same peptide moiety, when synthesized as cyclic peptide and dimerized via a PEG linker, was successfully used to block PLXNB1 signaling *in vivo* (33).

We found that the administration of Fc(m6A9)B3 efficiently reduced the growth of Py230 orthotopic tumors compared with Fc-treated controls (**Fig. 7A–C**). Analysis of tumor tissues of Fc(m6A9)B3-treated Py230 mice showed significant changes in the TME similar to those found in 4T1 tumor-bearing *Plxnb1*$^{-/-}$ mice. In particular, fewer $MRC1^+$ M2-like macrophages (Supplementary Fig. S6A) and enhanced recruitment of $CD8^+$ T cells and increased expression of GrzB (Supplementary Fig. S6B) were found in Fc(m6A9)B3-treated tumors compared with Fc control-treated tumors. This pharmacological targeting of PLXNB1 was well tolerated and impacted neither the hematological profile nor hepatic or renal functions (Supplementary Fig. S7A and S7B), when compared with untreated tumor-bearing mice.

To further assess whether genetic and pharmacological targeting of PLXNB1 would have similar antitumor effect in another independent TNBC mouse model, we injected EMT6 TNBC cells orthotopically in the mammary fat pad of syngeneic *Plxnb1*$^{-/-}$ Balb/c mice. We observed a significant inhibition of EMT6 tumor growth in *Plxnb1*$^{-/-}$ mice compared with WT controls (Supplementary Fig. S8A). In addition, we treated the EMT6 mouse model with Fc(m6A9)B3, and, similarly to the Py230 model, we observed a significant inhibition of tumor growth (Supplementary Fig. S8A).

Because a pharmacological systemic inhibition of PLXNB1 could also directly impact cancer cells in addition to reprogramming the

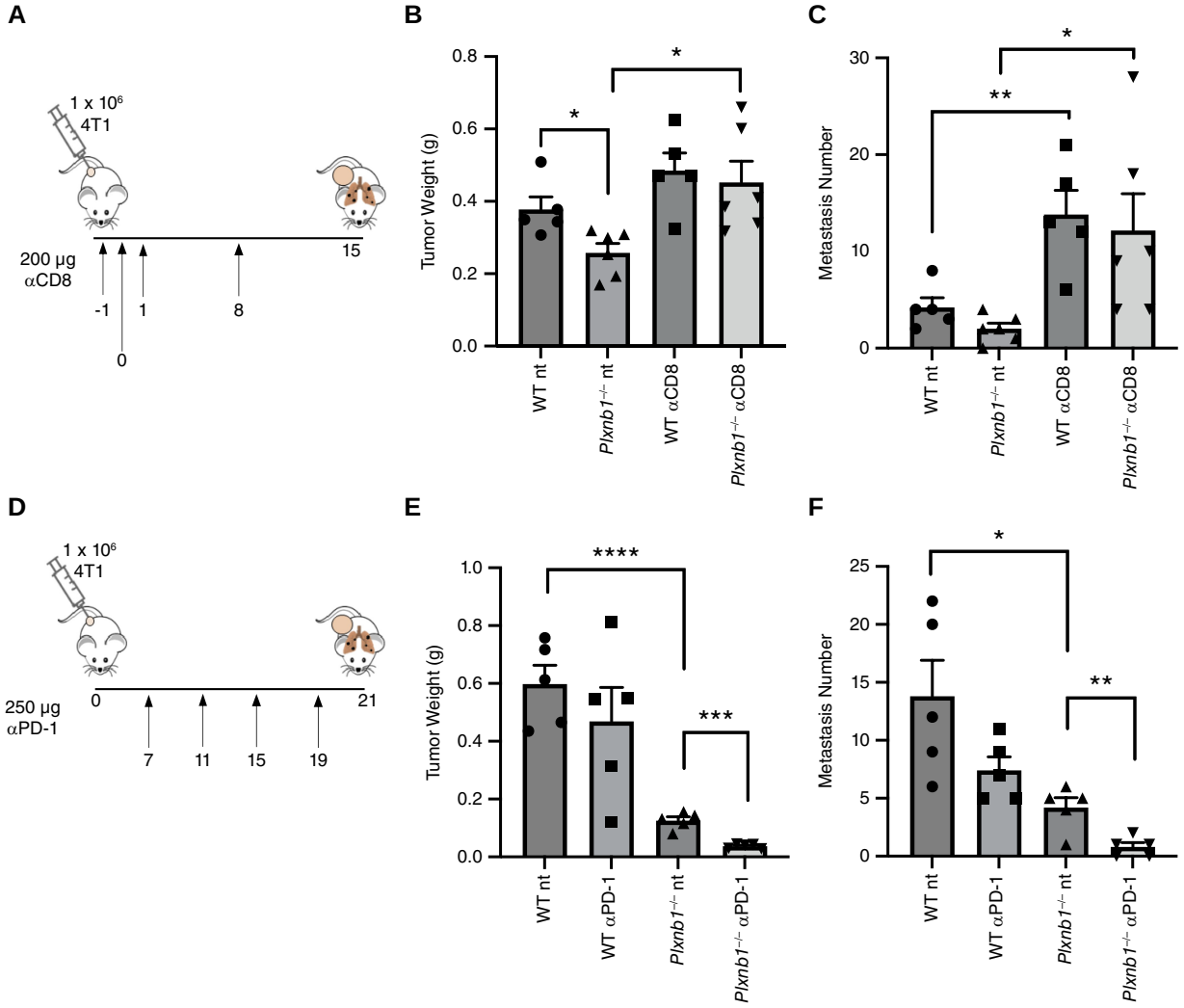

Figure 6.

PLXNB1 inactivation enhances the efficacy of anti-PD-1 immunotherapy hampering tumor growth. **A–C,** *CD8⁺ T-cell recruitment to tumors grown in Plxnb1*$^{-/-}$ *mice contributes to the reduction of tumor growth and metastatic burden.* **A,** Schematic representation of experimental design. 1×10^6 4T1 cells were injected in the mammary fat pad of female Balb/c WT and *Plxnb1*$^{-/-}$ mice at day 0. Anti-CD8 antibody treatment (200 µg IP) or saline solution as negative control (nt) was given at days −1, 0, 1, and 8. **B,** Bar graphs indicate average tumor weight ± SEM. **C,** Bar graphs indicate average lung metastasis number ± SEM. Results were analyzed by unpaired Student *t* test. *, $P < 0.05$; **, $P < 0.01$ ($n =$ at least 5 mice). **D–F,** *PLXNB1 inactivation enhances the efficacy of anti-PD-1 immunotherapy in 4T1 mice.* **D,** Schematic representation of experimental design. 1×10^6 4T1 cells were injected in the mammary fat pad of female Balb/c WT and *Plxnb1*$^{-/-}$ mice at day 0. Anti-PD-1 antibody treatment (250 µg IP) or saline solution as a negative control (nt) was given every 4 days starting from day 7. **E,** Bar graphs indicate tumor weight at explant ± SEM. **F,** Bar graphs indicate average lung metastasis number ± SEM. Results were analyzed by unpaired Student *t* test. *, $P < 0.05$; **, $P < 0.01$; ***, $P < 0.001$; ****, $P < 0.0001$ ($n = 5$ mice).

TME, we incubated Fc(m6A9)B3 with 4T1, Py230, and EMT6 TNBC cells in culture and observed no significant inhibition of cell viability (Supplementary Fig. S8B–D). Treatment of EMT6 tumor-bearing *Plxnb1*$^{-/-}$ mice with Fc(m6A9)B3 did not achieve any additional inhibition of tumor growth compared with Fc control-treated knockout mice (Supplementary Fig. S8A), suggesting that targeting PLXNB1 in the TME but not on the tumor cells is sufficient to achieve maximal tumor suppression. Finally, to assess whether Fc(m6A9)B3 could potentially induce ADCC, we performed an ADCC bioassay. Although the positive control Raji cells incubated with anti-CD20 yielded a strong ADCC response (estimated EC50 value = 43 ng/mL), no ADCC activity toward PLXNB1-expressing cells was detected upon incubation with Fc(m6A9)B3 (Supplementary Fig. S7C).

Based on the changes in the TME observed upon treatment with Fc(m6A9)B3 in TNBC models, we sought to investigate whether treatment with Fc(m6A9)B3 would enhance the antitumor efficacy of ICIs, as observed in the context of genetic depletion in 4T1 tumor-bearing *Plxnb1*$^{-/-}$ mice. Although PD-1 blockade in Py230 tumor-bearing mice could barely reduce the tumor burden, the combined treatment with Fc(m6A9)B3 and anti-PD-1 induced a greater antitumor effect compared with single treatments (**Fig. 7D** and **E**), suggesting that the two drugs unleash

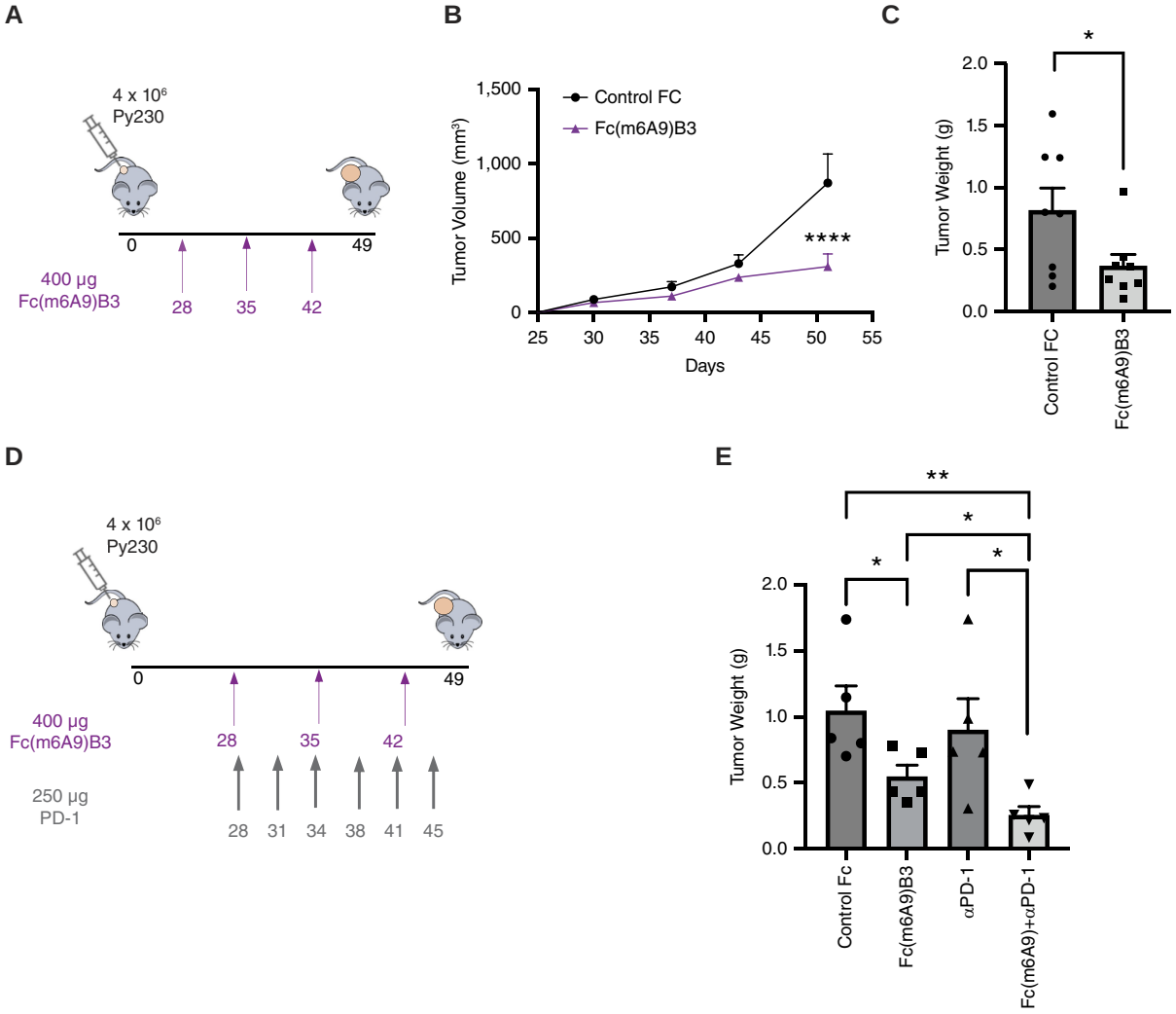

Figure 7.

Pharmacological inhibition of PLXNB1 inhibits tumor growth and synergizes with anti-PD-1 treatment. **A–C,** *Pharmacological inhibition of* PLXNB1 *reduces tumor growth.* **A,** Schematic representation of experimental design. 4 × 10^6 Py230 cells were injected in the mammary fat pad of female C57BL/6 mice at day 0. Fc(m6A9)B3 or Fc control was administered intravenously once a week for 3 weeks at a dosage of 400 µg starting at 4 weeks post Py230 tumor inoculation. **B,** Tumor growth curve. Results were analyzed by two-way ANOVA. ****, $P < 0.0001$ ($n = 8$ mice). **C,** Bar graphs indicate tumor weight at explant ± SEM. Results were analyzed by unpaired Student *t* test. *, $P < 0.05$ ($n = 8$ mice). **D** and **E,** *PLXNB1 blockade synergizes with anti-PD-1 treatment.* **D,** Schematic representation of experimental design. 4 × 10^6 Py230 cells were injected in the mammary fat pad of female C57BL/6 mice at day 0. Fc(m6A9)B3 or Fc control was administered intravenously once a week for 3 weeks at a dosage of 400 µg starting at 4 weeks post Py230 tumor inoculation. Anti-PD-1 antibody treatment (250 µg IP) was given twice a week starting at 4 weeks post tumor inoculation. **E,** Bar graphs indicate tumor weight at explant ± SEM. Results were analyzed by unpaired Student *t* test. *, $P < 0.05$; **, $P < 0.01$ ($n = 5$ mice).

complementary mechanisms suppressing tumor growth. Altogether, these data strongly suggest that both genetic and pharmacological targeting of PLXNB1 in diverse TNBC preclinical models efficiently suppresses tumor growth by reprogramming the immune response in the TME and thereby enhancing the antitumor efficacy of ICIs.

Discussion

The importance of semaphorin signaling in cancer onset and progression is raising increasing interest. The immune semaphorin SEMA4D, in particular, has been intensely studied in the tumor context, and its antibody-mediated blockade is currently being translated into the clinic (8, 9, 24). Moreover, it was shown that anti-SEMA4D can enhance the recruitment of activated monocytes and lymphocytes into the tumor, modifying the balance of stromal cells and cytokines in the TME toward a pro-inflammatory setting (8, 9). Intriguingly, the main receptor for SEMA4D, PLXNB1, is known to be expressed at varying levels in cancer cells; however, its role in the regulation of the TME has been poorly characterized so far.

Here, we show that the growth of three different TNBC models is strongly reduced in *Plxnb1*$^{-/-}$ mice compared with controls and that systemic treatment with a PLXNB1 inhibitor efficiently hampered tumor progression. PLXNB1 is expressed in all TNBC cells used in the

in vivo experiments but was also found in different cell populations in the TME, such as EC, myeloid, and T cells. Herein, we demonstrated, *in vivo* and *in vitro*, that PLXNB1 inhibition did not directly affect tumor cells but instead profoundly reprogrammed the TME of TNBC preclinical models. Thus, because SEMA4D inhibition has been shown to impinge on tumor growth and the TME in diverse mouse models (8, 9), we compared the growth of syngeneic 4T1 tumor cells orthotopically implanted in *Sema4d*$^{-/-}$ and in *Plxnb1*$^{-/-}$ mice. Although we detected a strong reduction of the tumor burden in both knockout mice, cancer growth suppression appeared particularly profound in *Plxnb1*$^{-/-}$ mice, suggesting that the efficacy of PLXNB1 targeting for cancer therapy is surely not inferior to SEMA4D inhibition or could even ensure a wider blockade of tumor-promoting ligands found in the TME. Even if the underlying mechanisms of this enhanced antitumor effect of PLXNB1 inhibition remain to be clarified, it may be conceivable that other Sema4s (e.g., Sema4A and/or Sema4C; ref. 34) can contribute to the observed effects.

Indeed, *in vivo* studies by Sierra and colleagues (7) demonstrated that tumor angiogenesis is reduced in tumors growing in a SEMA4D-deficient environment. However, in the PLXNB1 knockout model, we observed that tumor-induced angiogenesis was not affected. This is consistent with previous data and may be accounted for by the presence of alternative SEMA4D receptors (e.g., PLXNB2; ref. 17). We did observe an increase in vessel pericyte coverage upon PLXNB1 loss and a reduction in intratumoral hypoxia, suggestive of normalization of the tumor vasculature. Indeed, SEMA4D–PLXNB1 signaling has already been linked to vascular permeability alterations and in the regulation of pericyte function in rodent models of stroke and in a diabetic retinopathy model (35, 36). Moreover, a growing body of evidence demonstrated that the immune-vascular crosstalk and a mutual regulation between normalized vessels and T cells (37) can improve the efficacy of immunotherapy in cancer (38). Future experiments will aim at deciphering the precise molecular mechanisms responsible for this tumor vessel normalization and its potential involvement in the immune cell activation that we observed upon PLXNB1 depletion. At this stage, we sought to better characterize the differential immune infiltrate within tumors growing in *Plxnb1*$^{-/-}$ mice, finding an enhanced fraction of M1-polarized macrophages, compared with the TME of WT mice. Macrophages are one of the most represented immune cell populations in the TME and strongly impact on tumor growth and metastatic process. High density of TAM was significantly associated with late clinical staging in patients with BC, and TAMs are increasingly considered as a potential therapeutic target in BC (39). In addition, the inhibition of Arg-1 (M2 marker) and the trend toward enhanced expression of iNos (M1 marker) in BMDMs purified from *Plxnb1*$^{-/-}$ mice suggest that PLXNB1 may directly affect macrophage activity and polarization. In addition, we observed greater recruitment of CD11c^{+} cells in the TME of PLXNB1-deficient animals, suggestive of increased stromal infiltration of professional antigen-presenting cells compared with WT mice. Even though CD11c^{+} dendritic cells were more abundant in the TME of *Plxnb1*$^{-/-}$ mice, we cannot formally exclude that other subtypes could be present and functionally relevant in an environment lacking PLXNB1. Further experiments are needed to better characterize the diverse myeloid cell subtypes recruited in the absence of PLXNB1.

PLXNB1 has been found in activated human T lymphocytes (11) and dendritic cells (40). Our characterization of the lymphoid immune infiltrate showed it to be one of the most profound PLXNB1-dependent changes in the TME. In fact, we observed a strong increase in the amount of infiltrating CD8^{+} cytotoxic T cells in the TME of *Plxnb1*$^{-/-}$ mice. Although CD8^{+} cytotoxic T cells mediate tumor-specific adaptive immunity, CD4^{+} T helper cells exist in two main subtypes: Th1 and Th2. Th1 cells have a prominent antitumor activity due to their production of TNFα, IFNγ, IL2, and IL1. On the other hand, Th2 cells rather sustain tumor growth (41). Naive CD4^{+} T-cell differentiation into Th1 cells can be induced by STAT4, a transcription factor that we found induced in *Plxnb1*$^{-/-}$ TILs. Moreover, Th1 CD4^{+} T cells were increased in the PLXNB1-deficient TME compared with WT, and at the same time, tumor-infiltrating *Plxnb1*$^{-/-}$ CD8^{+} T cells showed an increased production of IFNɣ and GrzB and increased intratumoral proliferation, suggesting that PLXNB1 signaling may be involved in the inhibition of lymphocyte activation. The precise molecular mechanism for increased T-cell recruitment awaits elucidation, but a number of mechanisms can be proposed. On the one hand, increased TILs recruitment could be an indirect effect of increased pro-inflammatory macrophage or dendritic cell recruitment. On the other hand, PLXNB1 deficiency could be directly involved in regulating T-cell homing, as suggested by the altered expression of genes mediating T-cell activation and migration. We can speculate that PLXNB1 deficiency results in increased R-RAS signaling due to PLXNB1 intrinsic GAP activity (42). Previous work showed that R-RAS signaling plays a critical role in T-cell proliferation, migration, and activation (43). In line with what we observed in primary tumors, we noticed a significant recruitment of CD8^{+} T cells within the fewer lung metastases identified in 4T1 tumor-bearing *Plxnb1*$^{-/-}$ mice, which was barely detectable in WT controls. These findings suggest that PLXNB1 targeting induced profound changes in CD8^{+} T-cell activation and recruitment in the TME, which was appreciable not only in the primary tumor but also in distant sites, and may be partly accountable for the strong reduction of lung metastasis observed in tumor-bearing *Plxnb1*$^{-/-}$ mice. Although further experimental evidence in other preclinical models is warranted, these findings bear a remarkable potential relevance in clinical perspective. From a functional perspective, we wondered if the increase in CD8^{+} T cells could be sufficient to explain the PLXNB1-deficient mice phenotype. Upon anti-CD8 treatment, we found that the difference in growth and metastatic dissemination between tumors grown in *Plxnb1*$^{-/-}$ and WT mice was lost, rescuing the phenotype seen in WT animals. CD8^{+} T-cell targeting also impaired the metastatic ability of 4T1 tumors grown in WT mice, suggesting that cytotoxic T cells are fundamental in maintaining disease control in this model. Taken together, these data suggest that the enhanced CD8^{+} T-cell recruitment into tumors grown in *Plxnb1*$^{-/-}$ mice is mainly accountable for the suppression of tumor progression.

In line with the observed antitumor cytotoxic activity of CD8^{+} T cells, TIL gene expression analysis revealed that PLXNB1 deficiency was associated with the upregulation of T cell response genes such as *Icos* and *Perforin1*. *Ctla4* levels also were increased, possibly reflecting enhanced TCR signaling (44). Furthermore, *Stat3* and *Stat4* transcription factors were strongly induced, together with the chemokine *Ccl5*, a potent promoter of monocyte and T-cell migration. It should be noted that STAT3-deficient human CD8^{+} T cells fail to upregulate perforin and GrzB expression in response to IL21 and IL15 (45), whereas STAT4 is required for CD4^{+} T-cell differentiation into Th1 cells (46). In addition, we found that *Sele* (E-selectin) expression was strongly induced in *Plxnb1*-deficient T cells; this protein is usually expressed by ECs and participates in leukocyte rolling and adhesion to the endothelium (47). Interestingly, it has been previously shown that E-selectin can be induced by membrane TNFα in CD4^{+} T cells upon activation (48). Among the top down-modulated genes, we found *Vcam1*, an adhesion molecule expressed by thymocytes and

T cells undergoing apoptosis (49); *Fn1*, a major constituent of the extracellular matrix, synthesized by T cells upon activation (50); and *Cd34*, possibly suggesting a reduction in the recruitment of HSCs. T cells purified *ex vivo* from *Plxnb1*$^{-/-}$ mice carried an enhanced immune activation gene expression profile, compared with WT counterparts, a further indication that PLXNB1 inhibition directly affects T-cell function. In addition, in line with the differential gene expression observed in TILs, we found that *Plxnb1* silencing in stimulated T cells *in vitro* increased AKT signaling and STAT3 phosphorylation, indicative of enhanced activation of major pathways promoting T-cell expansion, survival, differentiation, and functional activity (51). We can speculate that PLXNB1 deficiency results in increased R-RAS or RAC1 signaling, which play a critical role in T-cell proliferation, migration, and activation (43, 52), potentially explaining the increased T cell-mediated immune response in PLXNB1-deficient tumors. For example, PLXNB1 loss might increase STAT3 activity by desequestering GTP-bound RAC1 in the cytosol or interfering with its activation (53, 54). Together, these data suggest that PLXNB1 deficiency appears to intrinsically stimulate T cells.

As a potential clinical application, we demonstrated for the first time that systemic pharmacological targeting of PLXNB1, using the targeted engineered inhibitor protein Fc(m6A9)B3, efficiently and safely inhibited cancer growth in two diverse TNBC models, faithfully recapitulating the results obtained in the gene-deficient mouse models, without inducing any toxic effect.

The TME of solid tumors is frequently defined as "cold" or "hot," based on the amount of T-lymphocyte infiltration and pro-inflammatory cytokine production. Hot tumors, characterized by higher levels of pro-inflammatory cytokines and T-cell infiltrate, display a better response to immunotherapies, such as ICIs targeting the PD-L1/PD-1 axis (3, 55). Hence, turning a cold tumor into a hot one has been in the focus of many recent therapeutic efforts, including for patients with BC. In our experiments, we found that PLXNB1 targeting enhances CD8$^+$ T-cell infiltration in both primary and metastatic sites, featuring their conversion into hot tumor tissues. Indeed, several trials employing anti-PD-1 as a new therapeutic strategy are ongoing for patients with TNBC (56). In this respect, although ineffective in 4T1 or Py230 tumor-bearing mice proficient for PLXNB1, a PD-1 blocking antibody treatment prompted a strong antitumor response in *Plxnb1*$^{-/-}$ mice and in mice systemically treated with the selective PLXNB1 inhibitor.

In conclusion, herein we unveil a specific role for PLXNB1 in regulating the TME of TNBC. Our results demonstrated that genetic or pharmacological targeting of PLXNB1 in TNBC models hampered cancer progression through reprogramming the TME toward a tumor-suppressor response, by recruiting and enhancing the activity of CD8$^+$ T cells, which in turn increased the efficacy of anti-PD-1 immunotherapy. These findings are promising from a translational perspective, providing preclinical evidence for new combination strategies with immunomodulatory agents and standard-of-care therapies for BC.

Authors' Disclosures

J. Takagi reports grants from Japan Agency for Medical Research and Development (AMED) during the conduct of the study and has a patent for WO2019026920A1 issued, licensed, and with royalties paid from MiraBiologics Inc. Dr. J. Takagi is a cofounder and shareholder of MiraBiologics Inc. No disclosures were reported by the other authors.

Authors' Contributions

G. Franzolin: Data curation, formal analysis, validation, investigation, methodology, writing–original draft. **S. Brundu:** Data curation, formal analysis, validation, investigation, methodology, writing–original draft. **C.F. Cojocaru:** Data curation, formal analysis, validation, writing–review and editing. **A. Curatolo:** Formal analysis, validation, investigation. **M. Ponzo:** Data curation, formal analysis, validation, investigation, methodology. **R. Mastrantonio:** Validation, investigation. **E. Mihara:** Data curation, formal analysis. **A. Kumanogoh:** Resources, writing–review and editing. **H. Suga:** Resources, methodology, writing–review and editing. **J. Takagi:** Resources, funding acquisition, methodology, writing–review and editing. **L. Tamagnone:** Conceptualization, resources, supervision, funding acquisition, methodology, writing–original draft, writing–review and editing. **E. Giraudo:** Conceptualization, data curation, supervision, funding acquisition, validation, methodology, writing–original draft, project administration, writing–review and editing.

Acknowledgments

The authors would like to thank Gabriella Cagnoni and Massimo Accardo for discussions and technical support. This work was supported by FPRC 5xmille Ministero Salute 2017 PTCRC-INTRA 2020, progetto SEE-HER to E. Giraudo; by Fondazione AIRC per la Ricerca sul Cancro (AIRC), IG #19957 and IG 2022 #27516 to E. Giraudo and IG #19923 and # 29255 to L. Tamagnone; by AIRC 5 per Mille, Special Program on Metastatic Disease (# 21052) to E. Giraudo and L. Tamagnone; by the Italian Ministry of Health, Ricerca Corrente 2022-23 to E. Giraudo and L. Tamagnone; and by the Platform Project for Supporting Drug Discovery and Life Science Research (22ama121011j0001) from the Japan Agency for Medical Research and Development (AMED) to J. Takagi. Università Cattolica del Sacro Cuore [Intramural Grant (Linea D1.1)] also contributed to the funding of this research project and to its publication.

Note

Supplementary data for this article are available at Cancer Immunology Research Online (http://cancerimmunolres.aacrjournals.org/).

Received April 4, 2023; revised March 15, 2024; accepted June 12, 2024; published first June 14, 2024.

References

1. Coughlin SS. Epidemiology of breast cancer in women. Adv Exp Med Biol 2019;1152:9–29.
2. de Visser KE, Joyce JA. The evolving tumor microenvironment: from cancer initiation to metastatic outgrowth. Cancer Cell 2023;41:374–403.
3. Duan Q, Zhang H, Zheng J, Zhang L. Turning cold into hot: firing up the tumor microenvironment. Trends Cancer 2020;6:605–18.
4. de Melo Gagliato D, Buzaid AC, Perez-Garcia J, Cortes J. Immunotherapy in breast cancer: current practice and clinical challenges. BioDrugs 2020;34:611–23.
5. Mastrantonio R, You H, Tamagnone L. Semaphorins as emerging clinical biomarkers and therapeutic targets in cancer. Theranostics 2021;11:3262–77.
6. Franzolin G, Tamagnone L. Semaphorin signaling in cancer-associated inflammation. Int J Mol Sci 2019;20:377.
7. Sierra JR, Corso S, Caione L, Cepero V, Conrotto P, Cignetti A, et al. Tumor angiogenesis and progression are enhanced by Sema4D produced by tumor-associated macrophages. J Exp Med 2008;205:1673–85.
8. Evans EE, Jonason AS, Bussler H, Torno S, Veeraraghavan J, Reilly C, et al. Antibody blockade of semaphorin 4D promotes immune infiltration into tumor and enhances response to other immunomodulatory therapies. Cancer Immunol Res 2015;3:689–701.
9. Clavijo PE, Friedman J, Robbins Y, Moore EC, Smith E, Zauderer M, et al. Semaphorin4D inhibition improves response to immune-checkpoint blockade

via attenuation of MDSC recruitment and function. Cancer Immunol Res 2019;7:282–91.
10. Chabbert-de Ponnat I, Marie-Cardine A, Pasterkamp RJ, Schiavon V, Tamagnone L, Thomasset N, et al. Soluble CD100 functions on human monocytes and immature dendritic cells require plexin C1 and plexin B1, respectively. Int Immunol 2005;17:439–47.
11. Granziero L, Circosta P, Scielzo C, Frisaldi E, Stella S, Geuna M, et al. CD100/Plexin-B1 interactions sustain proliferation and survival of normal and leukemic CD5+ B lymphocytes. Blood 2003;101:1962–9.
12. Conrotto P, Valdembri D, Corso S, Serini G, Tamagnone L, Comoglio PM, et al. Sema4D induces angiogenesis through met recruitment by Plexin B1. Blood 2005;105:4321–9.
13. Tamagnone L, Franzolin G. Targeting semaphorin 4D in cancer: a look from different perspectives. Cancer Res 2019;79:5146–8.
14. Fisher TL, Reilly CA, Winter LA, Pandina T, Jonason A, Scrivens M, et al. Generation and preclinical characterization of an antibody specific for SEMA4D. MAbs 2016;8:150–62.
15. Zuazo-Gaztelu I, Pàez-Ribes M, Carrasco P, Martín L, Soler A, Martínez-Lozano M, et al. Antitumor effects of anti-semaphorin 4D antibody unravel a novel proinvasive mechanism of vascular-targeting agents. Cancer Res 2019;79:5328–41.
16. Matsunaga Y, Bashiruddin NK, Kitago Y, Takagi J, Suga H. Allosteric inhibition of a semaphorin 4D receptor plexin B1 by a high-affinity macrocyclic peptide. Cell Chem Biol 2016;23:1341–50.
17. Fazzari P, Penachioni J, Gianola S, Rossi F, Eickholt BJ, Maina F, et al. Plexin-B1 plays a redundant role during mouse development and in tumour angiogenesis. BMC Dev Biol 2007;7:55.
18. Shi W, Kumanogoh A, Watanabe C, Uchida J, Wang X, Yasui T, et al. The class IV semaphorin CD100 plays nonredundant roles in the immune system: defective B and T cell activation in CD100-deficient mice. Immunity 2000;13:633–42.
19. Sugano-Nakamura N, Matoba K, Hirose M, Bashiruddin NK, Matsunaga Y, Yamashita K, et al. De novo Fc-based receptor dimerizers differentially modulate PlexinB1 function. Structure 2022;30:1411–23.e4.
20. Mihara E, Watanabe S, Bashiruddin NK, Nakamura N, Matoba K, Sano Y, et al. Lasso-grafting of macrocyclic peptide pharmacophores yields multifunctional proteins. Nat Commun 2021;12:1543.
21. Follenzi A, Naldini L. HIV-based vectors. Preparation and use. Methods Mol Med 2002;69:259–74.
22. Steenbrugge J, Vander Elst N, Demeyere K, De Wever O, Sanders NN, Van Den Broeck W, et al. Comparative profiling of metastatic 4T1- vs. non-metastatic Py230-based mammary tumors in an intraductal model for triple-negative breast cancer. Front Immunol 2019;10:2928.
23. Luque MCA, Gutierrez PS, Debbas V, Kalil J, Stolf BS. CD100 and plexins B2 and B1 mediate monocyte-endothelial cell adhesion and might take part in atherogenesis. Mol Immunol 2015;67:559–67.
24. Shafique MR, Fisher TL, Evans EE, Leonard JE, Pastore DRE, Mallow CL, et al. A phase Ib/II study of Pepinemab in combination with Avelumab in advanced non-small cell lung cancer. Clin Cancer Res 2021;27:3630–40.
25. Martin JD, Seano G, Jain RK. Normalizing function of tumor vessels: progress, opportunities, and challenges. Annu Rev Physiol 2019;81:505–34.
26. Ong CHC, Lee DY, Lee B, Li H, Lim JCT, Lim JX, et al. Hypoxia-regulated carbonic anhydrase IX (CAIX) protein is an independent prognostic indicator in triple negative breast cancer. Breast Cancer Res 2022;24:38.
27. Paijens ST, Vledder A, de Bruyn M, Nijman HW. Tumor-infiltrating lymphocytes in the immunotherapy era. Cell Mol Immunol 2021;18:842–59.
28. duPre' SA, Redelman D, Hunter KW Jr. Microenvironment of the murine mammary carcinoma 4T1: endogenous IFN-γ affects tumor phenotype, growth, and metastasis. Exp Mol Pathol 2008;85:174–88.
29. Duhen R, Fesneau O, Samson KA, Frye AK, Beymer M, Rajamanickam V, et al. PD-1 and ICOS coexpression identifies tumor-reactive $CD4^+$ T cells in human solid tumors. J Clin Invest 2022;132:e156821.
30. Voskoboinik I, Smyth MJ, Trapani JA. Perforin-mediated target-cell death and immune homeostasis. Nat Rev Immunol 2006;6:940–52.
31. Appay V, Dunbar PR, Cerundolo V, McMichael A, Czaplewski L, Rowland-Jones S. RANTES activates antigen-specific cytotoxic T lymphocytes in a mitogen-like manner through cell surface aggregation. Int Immunol 2000;12:1173–82.
32. Pusztai L, Karn T, Safonov A, Abu-Khalaf MM, Bianchini G. New strategies in breast cancer: immunotherapy. Clin Cancer Res 2016;22:2105–10.
33. Bashiruddin NK, Hayashi M, Nagano M, Wu Y, Matsunaga Y, Takagi J, et al. Development of cyclic peptides with potent in vivo osteogenic activity through RaPID-based affinity maturation. Proc Natl Acad Sci U S A 2020;117:31070–7.
34. Naito Y, Koyama S, Masuhiro K, Hirai T, Uenami T, Inoue T, et al. Tumor-derived semaphorin 4A improves PD-1-blocking antibody efficacy by enhancing $CD8^+$ T cell cytotoxicity and proliferation. Sci Adv 2023;9:eade0718.
35. Zhou Y-F, Li Y-N, Jin H-J, Wu J-H, He Q-W, Wang X-X, et al. Sema4D/PlexinB1 inhibition ameliorates blood–brain barrier damage and improves outcome after stroke in rats. FASEB J 2018;32:2181–96.
36. Wu J, Li Y, Chen A, Hong C, Zhang C, Wang H, et al. Inhibition of Sema4D/PlexinB1 signaling alleviates vascular dysfunction in diabetic retinopathy. EMBO Mol Med 2020;12:e10154.
37. Tian L, Goldstein A, Wang H, Ching Lo H, Sun Kim I, Welte T, et al. Mutual regulation of tumour vessel normalization and immunostimulatory reprogramming. Nature 2017;544:250–4.
38. Khan KA, Kerbel RS. Improving immunotherapy outcomes with anti-angiogenic treatments and vice versa. Nat Rev Clin Oncol 2018;15:310–24.
39. Qiu S-Q, Waaijer SJH, Zwager MC, de Vries EGE, van der Vegt B, Schroder CP. Tumor-associated macrophages in breast cancer: innocent bystander or important player? Cancer Treat Rev 2018;70:178–89.
40. Chabbert-de Ponnat I, Marie-Cardine A, Pasterkamp RJ, Schiavon V, Tamagnone L, Thomasset N, et al. Soluble CD100 functions on human monocytes and immature dendritic cells require plexin C1 and plexin B1, respectively. Int Immunol 2005;17:439–47.
41. Dushyanthen S, Beavis PA, Savas P, Teo ZL, Zhou C, Mansour M, et al. Relevance of tumor-infiltrating lymphocytes in breast cancer. BMC Med 2015;13:202.
42. Pasterkamp R. R-Ras fills another GAP in semaphorin signalling. Trends Cell Biol 2005;15:61–4.
43. Yan X, Yan M, Guo Y, Singh G, Chen Y, Yu M, et al. R-Ras regulates murine T cell migration and intercellular adhesion molecule-1 binding. PLoS One 2015;10:e0145218.
44. Guo J, Xue Z, Wang L. Transcriptional regulation of the immune checkpoints PD-1 and CTLA-4. Cell Mol Immunol 2022;19:861–2.
45. Kane A, Deenick EK, Ma CS, Cook MC, Uzel G, Tangye SG. STAT3 is a central regulator of lymphocyte differentiation and function. Curr Opin Immunol 2014;28:49–57.
46. Zhang Y, Zhang Y, Gu W, Sun B. Th1/Th2 cell differentiation and molecular signals. Adv Exp Med Biol 2014;841:15–44.
47. Milstone DS, O'Donnell PE, Stavrakis G, Mortensen RM, Davis VM. E-selectin expression and stimulation by inflammatory mediators are developmentally regulated during embryogenesis. Lab Invest 2000;80:943–54.
48. Harashima S, Horiuchi T, Hatta N, Morita C, Higuchi M, Sawabe T, et al. Outside-to-inside signal through the membrane TNF-alpha induces E-selectin (CD62E) expression on activated human CD4+ T cells. J Immunol 2001;166:130–6.
49. Ishiyama N, Kitagawa M, Takahashi H, Kina T, Hirokawa K. Expression of VCAM-1 in lymphocytes during the process of apoptosis. Pathobiology 1998;66:274–83.
50. Hauzenberger D, Martin N, Johansson S, Sundqvist K-G. Characterization of lymphocyte fibronectin. Exp Cell Res 1996;222:312–8.
51. Abdullah L, Hills LB, Winter EB, Huang YH. Diverse roles of akt in T cells. Immunometabolism 2021;3:e210007.
52. Celus W, Oliveira AI, Rivis S, Van Acker HH, Landeloos E, Serneels J, et al. PlexinA4 mediates cytotoxic T cell trafficking and exclusion in cancer. Cancer Immunol Res 2022;10:126–41.
53. Simon AR, Vikis HG, Stewart S, Fanburg BL, Cochran BH, Guan KL. Regulation of STAT3 by direct binding to the Rac1 GTPase. Science 2000;290:144–7.
54. Bulloj A, Maminishkis A, Mizui M, Finnemann SC. Semaphorin4D-PlexinB1 signaling attenuates photoreceptor outer segment phagocytosis by reducing Rac1 activity of RPE cells. Mol Neurobiol 2018;55:4320–32.
55. Esteva FJ, Hubbard-Lucey VM, Tang J, Pusztai L. Immunotherapy and targeted therapy combinations in metastatic breast cancer. Lancet Oncol 2019;20:e175–86.
56. Cortes J, Rugo HS, Cescon DW, Im S-A, Yusof MM, Gallardo C, et al. Pembrolizumab plus chemotherapy in advanced triple-negative breast cancer. N Engl J Med 2022;387:217–26.